Accepted Manuscript

SAFT- Force Field for the Simulation of Molecular Fluids 6. Binary and ternary mixtures comprising water, carbon dioxide, and *n*-alkanes

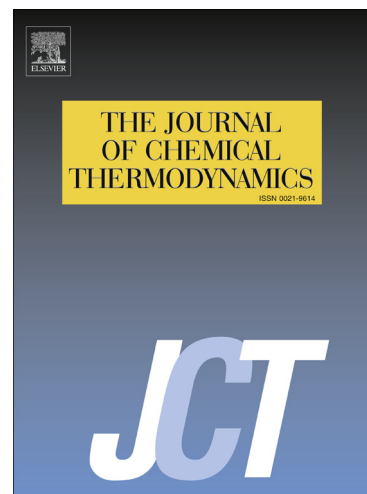Olga Lobanova, Andrés Mejía, George Jackson, Erich A. Müller

Please cite this article as: O. Lobanova, A. Mejía, G. Jackson, E.A. Müller, SAFT- Force Field for the Simulation of Molecular Fluids 6. Binary and ternary mixtures comprising water, carbon dioxide, and *n*-alkanes, *J. Chem. Thermodynamics* (2015), doi: http://dx.doi.org/10.1016/j.jct.2015.10.011

SAFT-γ Force Field for the Simulation of Molecular Fluids 6. Binary and ternary mixtures comprising water, carbon dioxide, and n-alkanes

Olga Lobanova[1], Andrés Mejía[2], George Jackson[1], Erich A. Müller[1]

[1]*Department of Chemical Engineering, Centre for Process Systems Engineering, Imperial College London, South Kensington Campus, London SW7 2AZ, United Kingdom*

[2]*Departamento de Ingeniería Química, Universidad de Concepción, POB 160-C, Correo 3, Concepcíon, Chile*

Abstract

The SAFT-γ coarse graining methodology [E. A. Müller and G. Jackson, Ann. Rev. Chem. Biomol. Eng. **5**, 405 (2014)] is used to develop force fields for the fluid-phase behaviour of binary and ternary mixtures comprising water, carbon dioxide, and n-alkanes. The effective intermolecular interactions between the coarse grained (CG) segments are directly related to macroscopic thermodynamic properties by means of the SAFT-γ equation of state for molecular segments represented with the Mie (generalized Lennard-Jones) intermolecular potential [V. Papaioannou, T. Lafitte, C. Avendaño, C. S. Adjiman, G. Jackson, E. A. Müller, and A. Galindo, J. Chem. Phys. **140**, 054107 (2014)]. The unlike attractive interactions between the components of the mixtures are represented with a single adjustable parameter, which is shown to be transferable over a wide range of conditions. The SAFT-γ Mie CG force fields are used in molecular-dynamics simulations to predict the challenging vapour-liquid and liquid-liquid fluid-phase equilibria characterising these mixtures, and to study properties that are not accessible directly from the equation of state, such as the interfacial properties. The description of the fluid-phase equilibria and interfacial properties predicted with the SAFT-γ Mie force fields is in excellent with the corresponding experimental data, and of comparable if not superior quality to that reported for the more sophisticated atomistic or united-atom models.

Keywords:

1. Introduction

Mixtures comprising water (H_2O), carbon dioxide (CO_2) and n-alkanes ($CH_3(CH_2)_nCH_3$) are of key importance due to their central role in the petrochemical industry. The systems are relevant in range of applications including enhanced oil recovery, CO_2 storage, natural gas transportation, crude-oil processing, and water purification. An accurate description of the phase behaviour of these mixtures is crucial for the optimal design of the corresponding chemical processes. From the modelling perspective, mixtures of water, n-alkanes, and carbon dioxide are challenging due to the disparate nature of interactions between the components which results in a highly non-ideal behaviour. While n-alkanes are non-polar, CO_2 possesses a significant quadrupole moment, while H_2O has a large dipole mo-

ment and also exhibits hydrogen bondings. The resulting mixtures are therefore highly asymmetric, both in terms of the molecular size and the energetic interactions. The disparity of the interactions is responsible for different types of global fluid-phase behaviour exhibited by mixtures of these species; binary mixtures of CO_2+H_2O [1, 2] and n-alkanes+H_2O [3, 4] are both characterized by type III behaviour (according to the classification of Scott and van Konynenburg [5, 6]), corresponding to extensive regions of liquid-liquid immiscibility and a discontinuous vapour-liquid critical line. In type III mixtures, the higher-temperature branch of the vapour-liquid critical line that starts at the critical point of the less volatile component merges with liquid-liquid critical line at higher pressures. The lower-temperature branch of the vapour-liquid critical line, which is usually much shorter, starts at the critical point of the more volatile component and merges with the vapour-liquid-liquid three-phase line at a upper critical end point (UCEP). Mixtures of carbon diox-

ide with long n-alkanes also display type III behaviour, whereas type II behaviour is observed with short n-alkanes [7, 8]. Type II behaviour is characterized by a continuous vapour-liquid critical line connecting the critical points of both pure components; the liquid-liquid critical line does not extend beyond the critical temperatures of either pure components, and merges with the three-phase line at an UCEP at lower presures.

The experimental phase diagrams of the aforementioned mixtures have been discussed by numerous authors. In particular, Schneider and co-workers [7, 8] have undertaken comprehensive studies of binary mixtures of n-alkane+CO_2, and n-alkane+H_2O systems has been the focus of the work of Brunner [3]. A large body of experimental data is now available on the fluid-phase behaviour of the CO_2+H_2O binary mixture, which has been summarized in reviews by Diamond and Akinfiev [9] and by Spycher *et al.* [10]. The most exhaustive studies at high temperatures and pressures were conducted by Todheide and Franck [1] and Takenouchi and Kennedy [2], however these data sets exhibit considerable inconsistency. Subsequent work has not completely resolved the discrepancies, although the data by Todheide and Franck [1] has been reported to exhibit errors in the composition of up to 1 mol % [10]. The absence of consistent experimental data introduces a degree of uncertainty in the characterization of these systems.

In terms of modelling, the use of cubic equations of state (EOSs) remains common practice in petrochemical engineering applications [11]. However, because cubic EOSs are fundamentally appropriate only for mixtures of near-spherical non-associating components, an accurate description of the fluid-phase equilibria is only possible if a number of empirical adjustable parameters are introduced, thereby curtailing the predictive capability of the approach. As an example, Cismondi *et al.* [12] have accurately described the fluid-phase behaviour of n-alkanes and carbon dioxide with a cubic EOS over a wide range of thermodynamic conditions by employing forty adjustable parameters.

In studies of associating mixtures such as aqueous mixtures of n-alkanes, it is highly advantageous to use an equation of state that can directly account for association. The statistical associating fluid theory (SAFT) [13, 14], which is based on the Wertheim formalism [15, 16, 17, 18, 19, 20], allows one to take both the directional nature of the hydrogen-bonding interactions and the non-sphericity (chain characteristics) of the molecules into account explicitly. A variety of variants of this molecular-based EOS have been developed over the last twenty five years including: SAFT for vari-

able range interactions (SAFT-VR) [21, 22, 23, 24]; SAFT for Lennard-Jones (LJ) based segments (soft-SAFT) [25]; perturbed-chain SAFT based on the structure of the hard-sphere chain (PC-SAFT) [26]; and the group contribution versions GC-SAFT [27, 28], SAFT-γ [29, 30, 31]), and GC-SAFT-VR [32]. In this context we should also mention that the Wertheim theory of association can also been coupled with a cubic EOS, as in the cubic plus association (CPA) approach [33]; this extends the applicability of traditional cubic EOS to associating fluids.

The various incarnations of the SAFT EOSs have been successfully applied to study mixtures of relevance to our current work comprising water, n-alkanes, and carbon dioxide. The main distinctive features of the fluid-phase equilibria of these systems can be accurately reproduced including: the transition from type II to type III phase behaviour exhibited by binary mixtures of n-alkanes+CO_2 with increasing carbon number [34, 35, 36]; the barotropic density inversion and solubility minima of water in carbon dioxide seen for CO_2+H_2O [37, 38, 39, 40, 41, 42, 43, 44, 45, 46]; and the solubility minima of the hydrocarbon in the water-rich phase [47, 48] and the extreme immiscibility found in n-alkane+H_2O mixtures [49, 50, 51, 52, 53, 54, 55, 56, 57]. There has been some controversy as to whether an unlike "association" interaction is required between carbon dioxide and water to account for the change of the slope in solubility near the critical temperature of CO_2 [37, 58] or whether this behaviour can be reproduced without the need for additional association interactions [40, 41, 42]. Explicit dipole and quadrupole moments have also been incorporated into a SAFT description of the intermolecular models for water and carbon dioxide [38, 39, 59, 60, 61, 62, 63, 64], with the advantage of providing a more physically detailed representation of the unlike interactions for the description of mixtures.

Although algebraic equations of state are still the preferred tool in the petrochemical community due to its computational efficiency, molecular-dynamics (MD) or Monte Carlo (MC) computer simulation techniques provide an insight at the microscopic level and allow one to study properties that cannot by accessed directly via an equation of state, such as interfacial and transport phenomena and the behaviour of the confined fluids [65, 66]. Molecular simulation essentially provides an exact numerical description of a system once the force field has been specified [67], and as a consequence the onus is on the development of accurate intermolecular potentials. The use of direct molecular simulation is becoming ever more prevalent as a consequence of

the steady increase of computational power [68] and the advances in modelling techniques [69].

Mixtures containing *n*-alkanes, carbon dioxide, and water have received considerable attention from a molecular simulation perspective. The quality of the description of the thermophysical properties obtained by molecular simulation depends critically on the underlaying intermolecular potential that is employed, particularly the unlike energetic interactions between the various components of the mixture. A variety of all-atom (AA) and united-atom (UA) classical (non-polarizable) force fields have been employed to study these mixtures with varying degrees of success; owing to the large body of research we mention only some representative examples of the more recent studies with a focus on fluid-phase equilibria to set our current work in the appropriate context.

Cui and Cummings [70] have used the Gibbs ensemble Monte Carlo (GEMC) simulation technique to determine the vapour-liquid equilibria (VLE) of binary mixtures of *n*-hexane+CO_2 using the elementary physical model (EPM2) of Harris and Yung [71] to represent carbon dioxide and the model developed by Siepmann, Karaborni, and Smit [72] (often referred to as SKS) for *n*-alkanes; the application of the common Lorentz-Berthelot (LB) geometric-mean combining rule for the unlike attractive dispersion interactions between the hydrocarbon groups and carbon dioxide was shown to provide a reasonable description of the mutual solubilities of the components in the coexisting phases for the thermodynamic states studies, with the largest deviations ($\sim 10\%$) seen for the liquid phase. In a grand canonical MC study of the global phase fluid-phase behaviour of *n*-hexadecane+CO_2 using a simplified LJ united atom model, Virnau *et al.* [73] have shown that the unlike interaction has to be reduced to $\sim 90\%$ of the LB value in order to represent the type III critical behaviour exhibited by the system.

The fluid-phase equilibria of a variety of mixtures comprising polar and non-polar species including carbon dioxide, *n*-alkanes, and water represented with UA exponential-6 (EXP-6) models have been simulated by Potoff *et al.* [74] using grand canonical histogram-reweighting MC; the LB combining rules employed for the unlike molecular interactions were found to be inappropriate in the case of mixtures comprising components with large differences in polarity. The focus of the subsequent GEMC study of Vorholtz *et al.* [75] was specifically on binary mixtures of carbon dioxide (represented with the EPM2 model) and water (represented with the three-site simple point charge SPC [76] and SPC/E [77] models, or with the four-site transfer-

able intermolecular potential TIP4P [78] model); the use of LB combining rules allowed for a reasonable description of the experimental fluid-phase equilibria only over a limited range of temperatures for supercritical conditions of carbon dioxide. One would not expect the LB combining rule to provide a good description of the thermodynamic properties of this non-ideal system [79], and a significant improvement can be achieved by adjusting the unlike CO_2−H_2O interaction (corresponding to a modification of the geometric-mean rule) [80]. Potoff and Siepmann [81] have proposed a model for carbon dioxide within the transferable potentials for phase equilibria (TraPPE) framework to determine the VLE of mixtures containing nitrogen, *n*-alkanes, and carbon dioxide, using both grand canonical MC and GEMC simulation. Two-centre LJ models with point quadrupoles (2CLJQ) have also been developed by Vrabec and co-workers [82, 83] to describe a broad variety of mixtures (including mixtures of carbon dioxide with nitrogen or light hydrocarbons) to a high level of accuracy by again making use of empirically adjusted unlike interactions.

The more challenging determination of the solubility of water in *n*-alkanes of increasing chain length (ranging from *n*-hexane to *n*-hexadecane and to longer polyethylene polymers) has been investigated by Johansson *et al.* [84] by GEMC simulation with the TraPPE model for *n*-alkanes [85] and the SPC model for water, using an empirical adjustment of unlike interaction to provide appropriate agreement with the experimental data; the inadequacy of the LB combining rule for these systems has also been noted in the recent work of Ballal *et al.* [86]. Motivated by earlier studies [87, 88, 89, 90], Ferguson *et al.* [91] determined the complementary solubility and molecular conformation of *n*-alkanes (ranging from ethane, C_2, to *n*-docosane, C_{22}) in water using the TraPPE model for *n*-alkanes and the SPC/E model for water with the usual LB combining rule for the unlike interactions; the aqueous solubilities of the hydrocarbons determined using the replica-exchange molecular-dynamics (REMD) technique together with an incremental Widom insertion scheme were found to be in excellent agreement with experiment up to *n*-decane, but did not support the break in the trend at *n*-undecane reported in the literature which the authors attributed to possible experimental artifacts owing to the very low solubilities of the longer hydrocarbons. It therefore appears that the LB recipe for the unlike water-alkane attractive interactions is sufficient to describe the solubility of *n*-alkanes in the water-rich phase but not of water in the hydrocarbon-rich phase.

A comprehensive study of the CO_2+H_2O binary mix-

ture has been reported recently in a series of papers by Panagiotopoulos and co-workers for the both the fluid-phase equilibria [92, 93] and transport properties [94, 95]; the performance of the various models for water (SPC, SPC/E, TIP4P, TIP4P2005, TIP4P/ϵ, and EXP-6) and CO_2 (EPM2, TraPPE, and EXP-6) were assessed with the overall conclusion that none of the force fields are capable of adequately reproducing the experimental fluid-phase equilibria over a broad temperature and pressure range. This is a good example of the fact that in spite of the relatively high-level of molecular detail, atomistic (non-polarizable) models are limited in terms of their transferability to different thermodynamic states and/or representability of different properties to the same accuracy. An appropriate choice of the unlike dispersion interaction between water and carbon dioxide applicable over a range of conditions is of central importance in this regard.

Within the last two decades, the use of a less-detailed coarse-grained (CG) description of intermolecular interactions is gaining popularity with the main purpose of enhancing the time and length scales computationally accessible for molecular systems of increasing size or complexity. The key to the success of a CG approach is the availability of reliable force fields. The most important requirements of CG models are their representability (of the various thermophysical properties), transferability (to broad thermodynamic conditions), and robustness (in the accuracy of the description of the target properties). The most common procedure for the development of CG force fields is to follow a "bottom-up" approach, where the unwanted degrees of freedom of a more detailed atomistic/molecular model are integrated out. For this purpose several techniques have been employed including iterative Boltzmann inversion [96], force matching [97, 98], and inverse Monte Carlo [99]. Unfortunately, one generally does not known *a priori* which degrees of freedom are important for the description of a given target physical property, and the CG parameter sets obtained in this manner are typically state, property, and system dependent.

By contrast, the SAFT-γ Mie "top-down" methodology [100] is followed in our current work, whereby an accurate molecular-based EOS, namely the SAFT-γ Mie EOS [31], is employed to develop reliable Mie (generalized LJ) CG force-field parameters directly from macroscopic experimental thermodynamic properties. The use of a high-fidelity EOS enables the simultaneous exploration of a wide parameter space for various target properties in order to estimate the optimal set of parameters that provide the optimal description of the experimental data.

The first use of the SAFT EOS within a top-down approach involved the parameterization of a model of water using a Wertheim TPT1 description complemented with a contribution to account for the dipolar interactions [59]. A generic top-down approach of this type has also been employed by Vrabec and co-workers [101, 102, 103]. In this case a semi-empirical EOS was developed by correlating a large set of volumetric and phase-equilibrium simulation data for two-center LJ (2CLJ) models which incorporate a dipole (2CLJD) or a quadrupole (2CLJQ) moment; the EOS was then used to develop reliable force fields for 78 pure components and 267 binary mixtures, including carbon dioxide and *n*-alkanes [83]. In a series of papers Elliot and co-workers have combined MD with high-temperature thermodynamic perturbation theory [104, 105, 106] within SAFT/SPEEDMD (for models based on the discontinuous square-well potential) [107, 108, 109, 110, 111] and, more recently, the SAFT-γ platform (for models based on the Mie potential) [112, 113] to successfully parameterize CG intermolecular potentials for a broad range of fluids including paraffins, olefins, aromatics, ethers, alcohols, and carboxylic acids. The PC-SAFT EOS has been used by van Westen *et al.* [114] to obtain force-field parameters for *n*-alkanes represented as chains of LJ segments; however, because the direct link between the intermolecular potential and the PC-SAFT description is partly lost, the final parameter set had to be obtained in an iterative manner by performing a number of additional simulations. Gross and co-workers [115, 116] have now refined the methodology for the development of transferable force fields for *n*-alkanes, olefins, and ethers based on the Mie potential by employing the PC-SAFT EOS to guide grand canonical MC simulations for the determination of the size and energy parameters.

The main advantage of using a framework based on the SAFT-γ Mie EOS [31] is that the link between the underlying intermolecular potential and the thermodynamic properties (through the Helmholtz free energy) is explicitly retained [24], thereby allowing one to estimate the CG force-field parameters reliably from the macroscopic properties of the system by direct parameter estimation with the analytical EOS. The SAFT-γ Mie top-down approach [100] has now been applied successfully to develop CG force fields for broad classes of molecular fluids including carbon dioxide [117], greenhouse gases [118], hydrocarbons [118, 119], aromatics [120], water [121], and aqueous solutions of nonionic [122], light-switching [123] and superspreading surfactants [124]. A corresponding states correlation can also be employed to parameterize models

4

for molecules represented as chains of Mie segments in cases where only limited experimental data is available [125], though the procedure is not generally appropriate to determine the intermolecular parameters between the different species in mixtures. Some of the SAFT-γ CG Mie force-fields previously developed for pure components have already been used successfully to simulate selected thermodynamic, interfacial and transport properties of numerous mixtures [126, 127, 128, 129, 130].

In our current paper we apply the SAFT-γ Mie methodology to obtain accurate estimates of the unlike dispersion interactions for binary mixtures containing n-alkanes, carbon dioxide, and water, thereby allowing for the global fluid-phase equilibria to be determined by direct MD simulation. The quality of the description of the mixtures is very sensitive to the specific interactions employed between the CG beads of the molecules, particularly in the case of the aqueous systems. Comparisons are made where possible with the corresponding results obtained using the more molecular detailed atomistic and united-atom models including explicit electrostatic interactions.

2. Methods and Models

2.1. SAFT-γ Mie coarse graining methodology

The SAFT-γ Mie EOS [31] provides a direct and robust link between the macroscopic and microscopic properties of the fluids. Our current paper is a part of a series of contributions on the development of the SAFT-γ CG force fields. These are based on the Mie intermolecular potential, which can be represented as

$$\phi^{Mie}(r) = C\epsilon\left[\left(\frac{\sigma}{r}\right)^{\lambda_r} - \left(\frac{\sigma}{r}\right)^{\lambda_a}\right], \tag{1}$$

where

$$C(\lambda_a, \lambda_r) = \left(\frac{\lambda_r}{\lambda_r - \lambda_a}\right)\left(\frac{\lambda_r}{\lambda_a}\right)^{\frac{\lambda_a}{\lambda_r - \lambda_a}}. \tag{2}$$

Here, λ_r and λ_a are the repulsive and attractive exponents, respectively, controlling the softness/hardness and the range of the attraction of the potential, σ is the length scale, related to the average diameter of the spherical segment, and ϵ is the energy parameter.

The force field characterizing the interactions between the molecular segments in the theory and the molecular simulations are based on the same Mie potential. The intermolecular parameters are determined by using the "top-down" approach, estimated by matching the experimental macroscopic bulk properties of the

fluid. The focus of of our work is the description of binary and ternary mixtures of water, carbon dioxide, and n-alkanes. For the three pure components, the saturated-liquid density and the vapour pressure are chosen as the target properties in the parameter estimation procedure [117, 121, 122]. For the sake of convenience, the parameter set is summarized in Table 1.

The CO_2 model is represented by a single-site CG sphere based on the Mie (23-6.66) potential, without any additional electrostatic interactions [117]. Despite the simplicity of the force field, with it one can accurately reproduce the entire phase envelope using a single parameter set. The prediction of properties which are not used in the parameterization procedure such as enthalpy of vaporization, interfacial tension, supercritical density, as well as the second-derivative thermodynamic properties (thermal expansion coefficient, isobaric heat capacity, isothermal compressibility, speed of sound, and Joule-Thomson coefficient) were found to be in a very good agreement with experimental data [117]. In a comprehensive study, which compared the thermodynamic properties of seven different force fields for carbon dioxide, Aimoli *et al.* [131] found that the SAFT-γ Mie force field provides a comparable accuracy to the higher-resolution force fields, including rigid and flexible atomistic three-site models.

The SAFT-γ CG Mie model of water is also based on the mapping of a single molecule to a single CG bead [121]. A spherical isotropic potential alone is not appropriate to provide an accurate physical representation of the interactions over a broad range of thermodynamic conditions as a consequence of averaging out the directional and electrostatic interactions of a highly polar and associating fluid such as water. Since the effective CG interactions between water molecules are found to vary significantly with temperature, temperature-dependent size and energy parameters are introduced. The saturation densities and vapour pressures can be accurately reproduced over a wide range of conditions using this set of temperature-dependent parameters. An alternative parameterization is necessary when the interfacial properties of water are of interest owing to the low level of resolution of the single-site model of water and the related issues of transferability with a CG procedure of this type [121].

The homologous series of n-alkanes are represented here as homonuclear chains of tangent Mie spherical CG segments. The development of CG models for long n-alkanes such as n-decane (n-$C_{10}H_{22}$) and n-eicosane (n-$C_{20}H_{42}$) has already been successfully demonstrated using the SAFT-γ Mie formalism [118]. The n-decane molecule was represented by three and n-eicosane by

5

Table 1: Intermolecular and intramolecular potential parameters of the SAFT-γ CG Mie force field for the pure components: m corresponds to the number of CG segments, σ is the segment size, ϵ is the energy parameter, and λ_r and λ_a are the repulsive and the attractive exponents, respectively, $\delta\rho$ % and δP % represent the percentage absolute average deviations (AAD %) between the description with the SAFT-γ Mie EOS and experimental saturated-liquid densities and vapour pressures for the temperature range from the triple point up to 90% of the critical point. The single-site CG model of carbon dioxide was developed in reference [117]. The size and energy parameters σ and ϵ of the single-site CG Mie water model are represented as polynomial function of temperature [121]: $\sigma(T)/\text{Å} = 1.262 \times 10^{-9}(T/\text{K})^3 - 8.720 \times 10^{-8}(T/\text{K})^2 - 4.554 \times 10^{-4}(T/\text{K}) + 3.119$ and $(\epsilon(T)/k_B)/\text{K} = 1.105 \times 10^{-5}(T/\text{K})^2 - 0.3077(T/\text{K}) + 586.8$.

intermolecular parameters							
like interactions							
Component	m	$\sigma/\text{Å}$	$(\epsilon/k_B)/\text{K}$	λ_r	λ_a	$\delta\rho$ %	δP %
CO_2	1	3.7410	353.55	23	6.66	1.71	19.48
H_2O	1	$\sigma(T)$	$\epsilon(T)$	8	6	0.03	0.01
n-alkanes							
n-C_5H_{12}	2	4.2449	310.78	15	6	0.51	0.48
n-C_6H_{14}	2	4.5089	342.00	15	6	0.43	6.26
n-C_7H_{16}	2	4.5736	380.87	15	6	11.46	17.24
n-C_8H_{18}	3	4.2412	321.65	15	6	1.16	2.12
n-C_9H_{20}	3	4.4212	344.83	15	6	0.30	3.85
n-$C_{10}H_{22}$	3	4.4908	363.99	15	6	5.48	9.25
n-$C_{11}H_{24}$	4	4.2212	328.18	15	6	1.11	3.04
n-$C_{12}H_{26}$	4	4.3635	344.42	15	6	0.22	1.33
n-$C_{13}H_{28}$	4	4.4680	354.25	15	6	0.42	2.06
n-$C_{14}H_{30}$	5	4.2332	329.81	15	6	5.04	6.99
n-$C_{15}H_{32}$	5	4.3286	344.85	15	6	0.71	2.13
unlike interactions							
Components i and j				$\lambda_{r,ij}$	$\lambda_{a,ij}$	k_{ij}	
CO_2 + H_2O				13.00	6.31	-0.07	
H_2O+n-alkane				10.75	6.00	0.36	
CO_2+n-alkane				18.50	6.31	0.08	
intramolecular parameters							
$k_{bond}/(\text{J mol}^{-1}\,\text{Å}^{-2})$		$r_0/\text{Å}$	$k_{angle}/(\text{J mol}^{-1}\,\text{deg}^{-2})$			$\theta/°$	
61.296×10^3		σ	5.38			159.9	

six fully flexible tangentially bonded Mie segments. A certain degree of parameter degeneracy in terms of overall performance is expected as a consequence of the conformal nature of the EOS description [132]. In our current work, we use an alternative CG mapping for n-alkanes developed in reference [122], where each segment was taken to represent three alkyl carbon backbone atoms and their corresponding hydrogen atoms. By applying this mapping, n-alkanes chains containing multiples of three carbon units can be represented directly: n-C_6H_{14}, n-C_9H_{20}, n-$C_{12}H_{26}$, n-$C_{15}H_{32}$, n-$C_{18}H_{38}$, etc. A good description of the thermodynamic properties of these alkanes is found to be provided with CG alkyl beads characterized by the Mie (15-6) potential. For convenience, the exponent pair (15-6) is also used to represent the interactions between the CG beads of the intervening alkanes considered here; the number of segments m is taken to be the nearest integer of the division of the carbon number C by three. The size and energy σ and ϵ parameters are then estimated from the experimental saturated-liquid density and vapour pressure of the individual alkanes following the usual SAFT-γ Mie procedure. The chosen mapping is by no means unique, as one can postulate parameter sets that fulfil other requisites, such as being "universal" across the entire homologous series [119] or correlated to the critical properties [125].

It is important to treat the degree of flexibility of chain molecules in an appropriate manner. In the case of n-alkanes it has been shown that a fully flexible model provides an accurate description the vapour-liquid equilibria and interfacial properties of the pure component system [118]. The effect of the chain flexibility has been examined recently in the context of the representation of n-alkanes with the SAFT-γ CG Mie force field [119]; a realistic description of the rigidity of the carbon backbone is necessary to accurately represent the structural and transport properties of the fluid. A physically realistic treatment of the semi-flexible nature of n-alkanes is also very important in the case of aqueous mixtures, where the solubility and structure of the hydrocarbon in water is found to be very sensitive to the degree of flexibility of chain molecules [122].

As with most of the other versions of the SAFT EOS, the SAFT-γ Mie EOS [31] used in our current work is based on the first-order thermodynamic perturbation theory (TPT1) of Wertheim [133, 20]. The specific geometry of the chain molecules is not predetermined at this level of the theory, although the approximations inherent in the TPT1 approach are expected to provide a more accurate description for elongated chains. This is beneficial when one considers a relatively rigid

alkyl backbone, described with realistic harmonic bond stretching and bond-angle bending intramolecular contributions:

$$U_{intra} = \frac{1}{2} \sum_{bond} k_{bond}(r - r_0)^2 + \frac{1}{2} \sum_{angle} k_{angle}(\theta - \theta_0)^2, \quad (3)$$

where k_{bond} and k_{angle} are the bond and the bending harmonic spring constants, respectively, and r_0 and θ_0 are the corresponding distance and angle at the potential minimum. The parameters for the intramolecular bonding interactions are also given in Table 1, and a detailed discussion of their determination is given in reference [119].

Simple combining rules are applied to describe the unlike interactions between the various components in the mixture [24]. The unlike size parameter σ_{ij} is obtained using the Lorentz arithmetic-mean combining rule:

$$\sigma_{ij} = \frac{\sigma_{ii} + \sigma_{jj}}{2}. \quad (4)$$

The unlike repulsive $\lambda_{r,ij}$ and unlike attractive $\lambda_{a,ij}$ exponents are both determined using the following relationship:

$$\lambda_{r/a,ij} - 3 = \sqrt{(\lambda_{r/a,ii} - 3)(\lambda_{r/a,jj} - 3)}, \quad (5)$$

which is consitent with the geometric mean of the van der Waals attractive constant [24]. The unlike energy parameter ϵ_{ij} is represented as

$$\epsilon_{ij} = (1 - k_{ij}) \frac{\sqrt{\sigma_{ii}^3 \sigma_{jj}^3}}{\sigma_{ij}^3} \sqrt{\epsilon_{ii}\epsilon_{jj}}, \quad (6)$$

where k_{ij} is an adjustable binary-interaction parameter, with $k_{ij} = 0$ taken as default to represent the commonly employed Berthelot geometric-mean combining rule (of the van der Waals constant). A proper prescription of the unlike energetic parameter is critical to adequately describe the interactions between different components [79]. Here we employ the SAFT-γ Mie EOS to estimate the k_{ij} parameter from appropriate experimental data of the given mixture in order to account for the differences in the attractive interactions between components. Although the binary k_{ij} parameter of the mixtures is adjusted to experimental fluid-phase equilibrium data at only one temperature, the choice is transferable to various thermodynamic conditions and is therefore applied to represent the entire phase diagram. A temperature dependence is already incorporated in the like interactions between water molecules, which allows one to capture the change in the interactions between the

components of the aqueous mixtures at different temperatures. The final set of molecular parameters (cf. Table 1), informed by the SAFT-γ Mie EOS, are used without modification in MD simulations.

2.2. Molecular dynamics simulation details

Two / three adjacent slabs of pure components located in a rectangular simulation box are taken as the initial configuration of a binary / ternary mixture, respectively, with standard periodic boundary conditions [67]. The fluid-phase equilibria is determined using MD simulation in the canonical ensemble (NVT), with constant number of particles N, volume V, and temperature T, using a temperature-quench algorithm [134]. Simulations of the liquid-liquid coexistence are initially carried out in the isobaric-isothermal NPT ensemble, with constant number of particles, temperature, and pressure P, for the sole purpose of allowing the system to attain densities close to the equilibrium values, followed by simulations in the NVT ensemble at the established equilibrium box dimensions to determine the average coexistence properties. The temperature of the system is fixed using a Nosé-Hoover thermostat [135, 136] with the coupling constant of 1.0 ps, and the pressure is maintained by means of a Parrinello-Rahman barostat with a relaxation constant of 10.0 ps. The equations of motion are integrated using the leap-frog algorithm [67] with a time step of 5 fs using the GROMACS 4.5.5 package [137]. A cutoff radius of 3.0 nm is used throughout for all of the interactions between the various CG Mie beads; a relatively large cutoff is necessary in order to retain the close correspondence with the theory [121]. As an initial configuration for the simulation of liquid-liquid equilibria (LLE), a phase separated system is assembled in the rectangular simulation box, with dimensions constrained to a minimum of 6 nm in x and y direction and four times larger in the z direction. The total number of particles is chosen according to the box dimensions. For the simulations of the VLE in the NVT ensemble, the z dimension is chosen to be approximately three times larger than for the LLE in order to cater for the low density of the vapour. After equilibrium has been established, the configurations are sampled for further 20 ns to determine the configurational average of the various properties. The composition of the fluid phases is estimated from the corresponding number density profiles of each component.

3. Results

For each of the binary mixtures studied, the unlike interaction parameter is adjusted to the fluid-phase equilibria at one thermodynamic state (isothermal slice) by matching the value predicted with the SAFT-γ Mie EOS to the corresponding experimental data. It is important to note that only a single binary adjustable parameter is required to account for the unlike energetic interactions between the components of the mixture over a wide range of conditions. The parameters determined in this way are used to investigate the entire fluid-phase behaviour (including VLE, LLE, critical lines, and three-phase lines) predictably using the SAFT-γ Mie EOS. Three-dimensional phase diagrams are produced to visualize the global phase behaviour. For the mixtures with n-alkanes, the same binary k_{ij} parameter is used to describe the unlike interactions between water or carbon dioxide and the alkyl beads for the components of different chain length. MD simulation of the fluid-phase equilibria are then carried out for the mixtures described with the CG force fields developed with SAFT-γ Mie EOS and the corresponding simulation data are compared critically with the experimental and theoretical results.

3.1. carbon dioxide+water binary mixture

The experimental data of Takenouchi and Kennedy [2] for the CO_2+H_2O mixture at a temperature of T = 473 K are employed to obtain the unlike energetic interaction parameter between the two components; the correlated pure-component data from the NIST database are also used in the analysis [138]. A value of $k_{ij} = -0.07$ estimated with the SAFT-γ Mie EOS is found to provide the best possible agreement with experimental data; this finding is consistent with the study of the CO_2+H_2O mixture carried out by Forte et al. [44] with the SAFT-VR EOS, and by Niño-Amézquita et al. [45] with the PCP-SAFT EOS. The quality of representation with the SAFT-γ Mie EOS is illustrated in Figure 1. The solubilities in both phases are reasonably well reproduced, including the solubility minimum of water in CO_2-rich phase.

The transferability of the force field can be validated by employing the same parameter set at temperatures which are not considered in the parameterization procedure. The adjustable parameter k_{ij} is treated as temperature-independent and appears to be transferable to different conditions (e.g., at T = 383 K as seen in Figure 1). For this temperature the phase compositions and the solubility maximum are accurately captured at lower pressures. At high pressures, the deviations become more apparent. Overall, the corresponding data obtained by MD simulations performed at the same thermodynamic conditions agree well with the theoretical predictions.
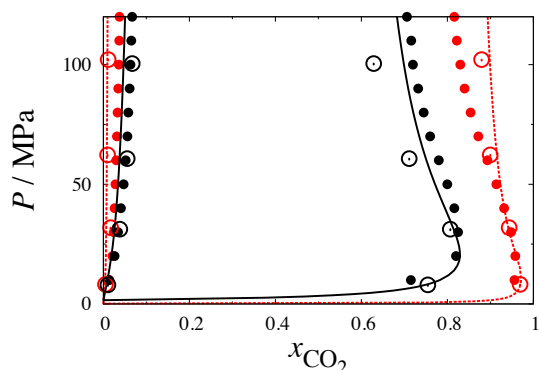
Figure 1: Isothermal pressure-composition (Px) slices of the fluid-phase equilibria for the carbon dioxide+water binary mixture at temperatures of $T = 383$ K (red/dashed) and 473 K (black/continuous). The filled circles correspond to experimental fluid-liquid equilibrium data [2]. The curves represent the calculations with the SAFT-γ Mie EOS [31] using the parameters given in Table 1. The empty circles represent the corresponding predictions of the phase boundaries obtained with our SAFT-γ Mie CG force field by direct molecular-dynamics simulation.

The entire fluid-phase behaviour for the system with the unlike interaction parameter $k_{ij} = -0.07$ can be determined easily with the SAFT-γ Mie EOS. The CO_2+H_2O mixture exhibits type III phase behaviour according to the classification of Scott and van Konynenburg [5, 6], which is characteristic of highly immiscible fluids. The global features of the fluid-phase behaviour, which is displayed in Figure 2, is indeed dominated by extensive regions of fluid immiscibility.

The discontinuous vapour-liquid critical line can also be seen in the PT projection of the PTx surface shown in Figure 3. The critical line at the intermediate pressures is in good agreement with experimental data but there are larger deviations at higher pressures. The lower branch of the vapour-liquid critical line merges with the three-phase line in the UCEP; the three-phase line is at pressures slightly lower than the vapour-pressure curve of pure carbon dioxide. The critical point of the CO_2 is overestimated by the SAFT-γ CG Mie model [117] due to the mean-field nature of the theory, which in turn leads to a slight overestimation of the pressures of three-phase coexistence with the SAFT-γ Mie EOS. A clearer representation of the three-phase
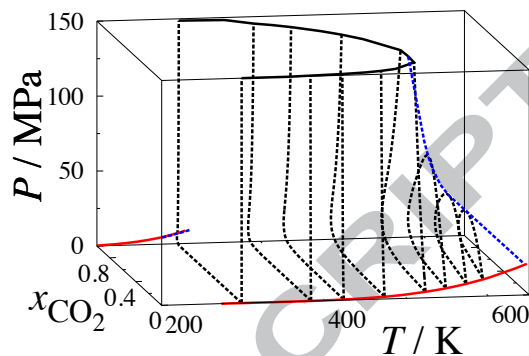

Figure 2: Three-dimensional pressure-temperature-composition (PTx) surface of the fluid-phase equilibria for the carbon dioxide+water binary mixture predicted with the SAFT-γ Mie EOS [31] using the parameters given in Table 1. The continuous red curves on opposing faces of the prism represent the vapour-pressure curves of the pure components, the dashed blue curves are the critical lines and the PT projection of the three-phase line, and the dashed black curves correspond to isothermal pressure-composition (Px) sections.

line and the lower branch of the critical line is illustrated in the inset of Figure 3.

The three-phase line separates the liquid-liquid equilibrium at higher pressures from the vapour-liquid equilibrium at lower pressures; at the three-phase line, two immiscible liquid phases coexist with the vapour phase. In Figure 4, the isothermal pressure-composition (Px) slice at a temperature of $T = 298$ K predicted with the SAFT-γ Mie EOS is compared to the corresponding experimental data [139, 140, 141, 142, 143, 144]. The vapour-liquid equilibrium is in very good agreement with experiment; at the liquid-liquid equilibrium conditions, the concentration of carbon dioxide is slightly underestimated in both phases. The three-phase pressure is reproduced within a deviation of 0.45 MPa compared to the experimental value. A small vapour-liquid region with a CO_2-rich vapour in coexistence with a CO_2-rich liquid phase is observed above the three-phase line. The theory is able to capture the main features of the CO_2+H_2O mixture at this temperature, providing an explanation to the solubility minimum of water in the CO_2-rich phase at higher temperatures: the solubility minimum is clearly ascribed to the proximity of the three-phase line. At low temperatures, the solubility curve exhibits a sharp discontinuity at the three-phase coexistence pressure, and as the temperature increases
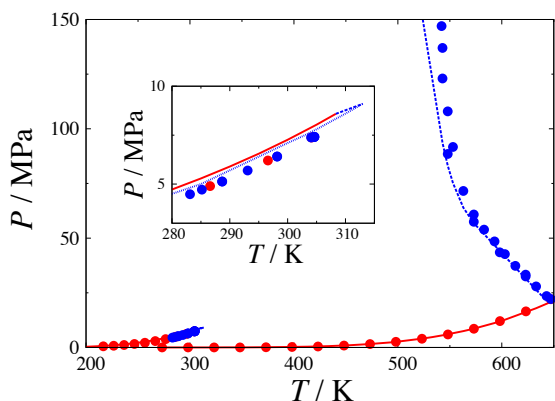
9

Figure 3: Pressure-temperature (*PT*) projection of the fluid-phase equilibria for the carbon dioxide+water binary mixture. The red circles correspond to the experimental vapour pressures of the pure components [138], the blue circles correspond to the experimental vapour-liquid critical line and three-phase line [1, 2]. The curves represent the description with the SAFT-γ Mie EOS [31] using the parameters given in Table 1: the continuous red curves are the calculations for the vapour pressures of the pure components, the dashed blue curves are the predictions for the vapour-liquid critical lines and three-phase line. The region close to the critical point of pure carbon dioxide is shown enlarged in the inset.

above the UCEP, the discontinuity disappears thereby causing a minimum at pressures close the UCEP. This behaviour is described in greater detail in reference [40]

The MD simulations reproduce the theoretical predictions very accurately (cf. Figure 4). The three-phases – the H_2O-rich liquid phase (L_1), the CO_2-rich liquid phase (L_2), and the gaseous phase (G) – can be clearly distinguished in the corresponding density profile and the snapshot, presented in Figure 5. The adsorption of CO_2 at the interface between the L_1 and L_2 phases is distinctly featured in the density profile. The CG model of H_2O employed in our study represents accurately the volumetric properties at the expense of only providing qualitative agreement for the interfacial tensions. For accurate values of the interfacial properties, a different parameter set should be employed [121]. The predictive capabilities of the aformentioned SAFT-γ CG Mie models are accurate enough in aiding to detect errors and discern between conflicting experimental data sets [145].
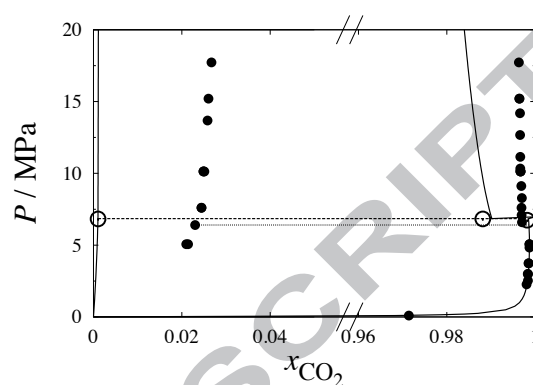

Figure 4: Isothermal pressure-composition (*Px*) slice of the fluid-phase equilibria for the carbon dioxide+water binary mixture at a temperature of T = 298 K. The filled circles correspond to experimental vapour-liquid and liquid-liquid equilibria [139, 140, 141, 142, 143, 144]. The dotted line represents the experimental three-phase line. The continuous curves represent to the predictions of the SAFT-γ Mie [31] using the parameters given in Table 1, and the dashed line is the three-phase line. The empty circles represent the corresponding three-phase line compositions predicted with our SAFT-γ CG Mie force field by direct molecular-dynamics simulation.

The adsorption phenomena at the liquid-liquid interface can be studied via MD simulations at different temperatures and pressures. The density profiles at temperatures of T = 383 and 423 K are presented in Figure 6 at pressures of P = 8.18, 31.87, 62.30, and 102.10 MPa. The density profile of H_2O is not very sensitive to pressure and is therefore shown only at one pressure for clarity. CO_2 exhibits a positive surface activity ($d\rho_{CO_2}/dz$ = 0, $d^2\rho_{CO_2}/dz^2$ < 0), whereas H_2O does not. The surface activity of CO_2 increases as the pressure increases until the limiting bulk liquid density is reached and saturation is established. A lower surface activity and the widening of the interface produced by a decreased in the slope of the CO_2 density curve is observed with increasing temperature.

Apart from the interfacial behaviour, the pressure dependence of the bulk densities of the CO_2+H_2O mixture are of scientific interest as the mixture exhibits mass barotropy (density inversion). In this phenomenon, the supercritical CO_2 phase becomes denser than the H_2O phase at high pressures, so that two phases change their positions in a gravitational field. The experimental den-
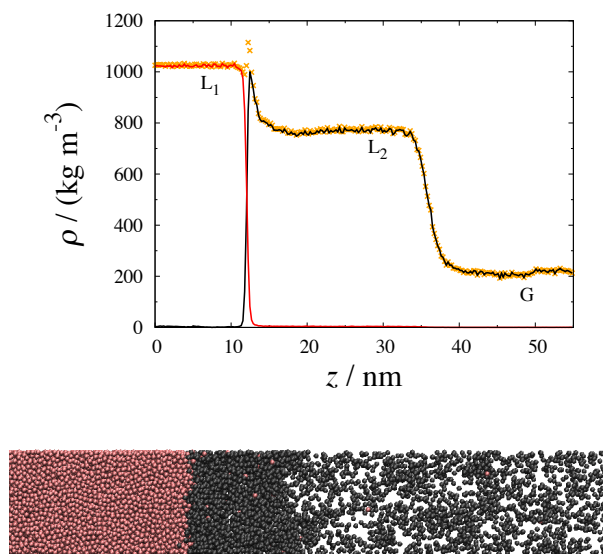
10

Figure 5: Total density profile (yellow crosses) of the carbon dioxide+water binary mixture at three-phase co-existence corresponding to a temperature of $T = 298$ K and a pressure of $P = 6.82$ MPa obtained with our SAFT-γ Mie CG force field by direct molecular-dynamics simulation using the parameters given in Table 1. L_1 denotes the water-rich liquid phase, L_2 denotes the carbon dioxide-rich liquid phase, G denotes the gas phase. In the snapshot of a representative configuration during the simulation, the water molecules are displayed in red (red density profile in upper panel) and the carbon dioxide molecules in black (black density profile in upper panel).

sities of the mixture [146] are compared to the predictions with the SAFT-γ Mie EOS and MD simulations at temperatures of $T = 298$, 304, 383, 423, and 473 K in Figure 7. The theoretically calculated densities of the CO_2-rich phase are in excellent agreement with experiment, both in the sub- and the super-critical region, whereas the densities in the H_2O-rich phase are slightly underestimated. The pressures at which the barotropic density inversion occurs, at a given temperature, are compared to the experimental values [1] in Table 2. Taking into account that these are predictions with very simple models using only one adjustable unlike interaction parameter, the agreement between theoretical predictions and experimental data is quite encouraging. The MD simulation data accurately reproduce the values predicted with the SAFT-γ Mie EOS (and thereby the experimental data).

Table 2: Barotropic density inversion points for the carbon dioxide+water binary mixture measured experimentally [1] and predicted with the SAFT-γ Mie EOS [31] using the parameters given in Table 1.

T / K	P_{EXP} / MPa	P_{SAFT} / MPa
323	80	70
373	125	108
523	200	161

The description of the fluid-phase equilibria for the CO_2+H_2O mixture obtained with our SAFT-γ CG Mie models can also be compared to the corresponding results of the atomistic simulations determined by Liu *et al.* [92] for some of the popular force fields for H_2O (SPC, TIP4P, TIP4P2005, and exponential-6) and CO_2 (EPM2, TraPPE, and exponential-6) using LB combining rules to describe the unlike pair interactions. The simulated data is used to assess the contradictory experimental data reported by Todheide and Franck [1] and by Takenouchi and Kennedy [2].

Two isothermal slices of the *PTx* fluid-phase equilibrium surface are examined in Figure 8: one at $T = 423$ K corresponds to the region well below the critical point of water and the other to the near-critical region ($T = 548$ K). Due to considerable disagreement between the experimental data sets, it is difficult to judge which model delivers the best performance. The representation with our SAFT-γ CG Mie force field is in closer agreement with the experimental data of Takenouchi and Kennedy [2], clearly exhibiting a solubility minimum at low pressures, which appears due to the proximity of the three-phase line at low temperatures, as discussed earlier. The solubility minimum is not reproduced by any of the atomistic models. When compared with the experimental data of Todheide and Franck [1], the best performance is achieved by the exponential-6 models for the CO_2-rich phase and TraPPE/TIP4P2005 model for the H_2O-rich phase at $T = 423$ K. At high temperatures, the exponential-6 models perform better than the other atomistic models: the lower part of the phase envelope can be accurately reproduced, whereas the critical pressure is largely underestimated compared to both sets of experimental data. The SAFT-γ Mie CG models exhibit a similar behaviour, with good agreement with experiment at low pressures but larger deviations and an underestimation of the critical point at high pressures. Despite the high level of molecular resolution of the atomistic models one cannot adequately reproduce the fluid-phase behaviour over a wide temperature and pressure range: at low temperatures, the

11

solubility in the both phases cannot be reproduced simultaneously; at high temperatures, only a qualitative description can be achieved with atomistic models. On that account, the performance of the SAFT-γ Mie CG models can be considered at least as good if not better than the atomistic models. The main issue with the atomistic force fields is the use of conventional LB combining rules for the dispersion interactions between unlike components of the mixture; an improved description could certainly be obtained by refining the unlike attractive interaction, though this typically requires an iterative simulation procedure. Having a direct robust simultaneous link between theory, experiment, and simulation enables one to assess the adequacy of the force-fields in describing the fluid-phase behaviour over a wide range of conditions with greater confidence.

3.2. n-alkane+water binary mixtures

The approach described in the previous section is applied to study aqueous mixtures of n-alkanes which are characterized by broad regions of extreme liquid-liquid immiscibility. A binary interaction parameter of $k_{ij} = 0.36$ for the CG energetic interaction between the H_2O and alkyl beads is estimated from the solubility of H_2O in a coexisting n-hexane-rich liquid phase at a temperature of $T = 473$ K. The quality of the theoretical representation of the experimental VLE and LLE reported in Refs. [147, 148, 149] is illustrated in Figure 9. The n-hexane+water mixture exhibits a heteroazeotrope, where the vapour phase coexists with two immiscible liquid phases. The azeotropic point is accurately captured by the SAFT-γ Mie EOS both in terms of composition and pressure at the given temperature. MD simulations of our CG force field are seen to correctly reproduce the solubility of water in hexane-rich liquid phase. The compositions of both phases in vapour-liquid equilibria are also accurately captured by the simulations. The simulated values for the phase composition at the azeotropic point display remarkable agreement with the theoretical prediction and the experimental data. The corresponding density profile of the mixture at the temperature of $T = 473$ K and pressure of $P = 3.33$ MPa is illustrated in Figure 10. Three phases – a H_2O-rich liquid phase L_1, an n-hexane-rich liquid phase L_2, and a gas phase G – are clearly distinguishable from the densities of the bulk regions, which can also be seen in the snapshot of a representative configuration from the MD simulation.

The solubility of water in the n-hexane-rich liquid phase at LLE is accurately captured by the SAFT-γ Mie CG parameter set developed in our current work,

both by the equation of state and by molecular simulation. The concentration of n-hexane in the H_2O-rich liquid phase is however very low and represents a challenge for any modelling technique. Whereas the experimental mole fractions are of the order of 10^{-6} ($x_{C_6H_{14}} = 1.5 \times 10^{-6}$) [147], the prediction with the SAFT-γ Mie EOS is $x_{C_6H_{14}} = 4.8 \times 10^{-9}$. Gratifyingly, the MD simulation of an equilibrium drop of n-hexane in bulk water described with our SAFT-γ Mie CG force field yields a solubility of $x_{C_6H_{14}} = 3.3 \times 10^{-5}$; the reader is referred to reference [122] for details of the procedure employed. The modelling techniques may require refinement and a more sophisticated analysis, however it is encouraging that the order of magnitude of the experimental values is reasonably well reproduced.

Using a value of $k_{ij} = 0.36$ for the unlike CG interactions between the H_2O and alkyl beads, we extend the prediction to study the rest of the fluid-phase diagram. The family of n-alkanes+H_2O mixtures is known to exhibit type III behaviour [3]. The extent of the liquid-liquid immiscibility gap can be visualized in the three-dimensional PTx phase diagram in Figure 11. The discontinuity of the vapour-liquid critical line is clearly seen in the corresponding PT projection shown in Figure 12. The description of the UCEP with the SAFT-γ Mie EOS on the low-temperature branch of the vapour-liquid critical line is slightly overestimated compared to experimental data due to the overprediction of the critical point for n-alkanes, which is apparent from the inset of Figure 12. In heteroazeotropic systems of this type, the three-phase line is located at higher pressures than the vapour pressure of either of the pure components. As was already evident from Figure 9, the prediction of the three-phase line is in excellent agreement with the experimental data. The upper branch of the vapour-liquid critical line should exhibit a minimum typical for the systems with the gas-gas immiscibility of the second kind [150]. However, our calculations do not capture the change of the slope of the critical line thereby suggesting a gas-gas immiscibility of the first kind, characteristic for systems with even greater disparity of the intermolecular forces.

The interfacial profiles can be studied by MD simulation at pressures corresponding to the vapour-liquid and liquid-liquid equilibria. The interfacial region of the n-hexane+H_2O mixture is shown in Figure 13 at a temperature of $T = 473$ K and pressures below ($P = 2.16$ and 2.87 MPa) and above ($P = 6.25$ MPa) the three-phase line. As in the mixture with CO_2, in mixtures with n-alkanes, H_2O does not exhibit any surface activity, $i.e.$, the average density profile has a monotonic hyperbolic shape. By contrast, at pressures below the three-phase

Table 3: Experimental bulk density ρ data at liquid-liquid equilibrium for the n-hexane+water binary mixture at a temperature of $T = 373.15$ K. The standard uncertainties of the measurments are: $\rho \pm 0.4$kg m^{-3}; $T \pm 0.1$ K; and $P \pm 0.1$ MPa.

	n-hexane-rich phase	water-rich phase
P/MPa	ρ/(kg m^{-3})	ρ/(kg m^{-3})
0.675	582.196	959.325
2.762	587.029	960.684
5.297	592.773	962.144
7.738	597.693	963.656
10.156	602.218	965.110
12.625	606.434	966.573
15.100	610.365	968.074
17.655	614.461	969.517
20.142	618.210	970.994

line, n-hexane exhibits a positive surface activity which increases as the pressure is increased. Above the three-phase line pressure, n-hexane reaches the bulk liquid density and does not show any activity at the interface. One can clearly see the progression of the adsorption of n-hexane onto the water surface in Figure 13. At low pressures a small surface excess is present, which grows into a liquid-like film that eventually becomes a bulk liquid phase at sufficiently high pressures.

Due to the lack of appropriate experimental data for the densities of the coexisting phases of the n-hexane+H$_2$O mixture at the conditions of interest, we perform measurements in our current work. The mass densities of the mixture are measured at a temperature of $T = 373.15$ K over the pressure range $P = 0.6$ to 20 MPa by using a stainless steel high-pressure LLE cell and a DMA HP densimeter (Anton Paar GmbH, Austria) with an accuracy of 5×10^{-3} kg m^{-3}. Details of the experimental procedure are given in Appendix, and the densities are summarized in Table 3.

From the modelling perspective, the bulk densities can be obtained both by using the SAFT-γ Mie EOS of by direct molecular-dynamics simulation. The calculated densities of n-hexane+H$_2$O mixture are compared to the experimental data in Figure 14. A barotropic density inversion for the n-hexane+H$_2$O is expected only for long-chain alkanes, starting from n-octacosane (n-C$_{28}$H$_{58}$) [3], and therefore is not observed in the case of n-hexane. A very good agreement between the densities predicted by the SAFT-γ Mie EOS, the MD simulations, and the experiment data is observed at $T = 373$ K; the MD simulations are also seen to reproduce the theoretical results with high accuracy at $T = 473$ K.

The wealth of data available for aqueous alkanes provides a testing ground for the transferability of the model. If the force field is transferable, the unlike interaction parameter which has been adjusted to reproduce the fluid-phase equilibria of the n-hexane+H$_2$O mixture should also provide a quantitative agreement with experiment for mixtures involving the other n-alkanes. The experimental data for the n-dodecane++H$_2$O mixture is assessed at a temperature of $T = 603$ K, which is above the UCEP. The the SAFT-γ Mie EOS captures both the low-pressure region of VLE and the high-pressure region of LLE (cf. Figure 15). The MD simulations of the system represented with the SAFT-γ CG Mie force field given in Table 1 are found to reproduce the theoretical values with reasonable accuracy for both the VLE and LLE phase boundaries. The three-dimensional PTx fluid-phase diagram obtained with the SAFT-γ Mie EOS is presented in Figure 16. The discontinuity of the vapour-liquid critical line can be visualized in PT-projection in Figure 17. As for the n-hexane+H$_2$O mixture, the three-phase line is in excellent agreement with experiment. Due to the overprediction of the critical point of the n-alkanes, the critical pressure close to the critical point of n-dodecane is overpredicted and the minimum in the upper branch of the critical line is not reproduced. Nevertheless, the parameter set is capable of representing the main features of the fluid-phase equilibria and is transferable not only to different conditions but also to others members of the homologous series of the n-alkanes.

3.3. n-alkane+carbon dioxide binary mixtures

Binary mixtures of n-alkane and CO$_2$ are particularly interesting because the fluid-phase equilibria exhibits a change from type II to type III behaviour on increasing the chain length of the n-alkane. Capturing this feature with only one adjustable parameter for the entire homologous series is a challenging task for any equation of state [34]. A value of the binary parameter of $k_{ij} = 0.08$ between the unlike interaction between the CO$_2$ and alkyl CG beads is found to provide a good match with experimental data of the vapour-liquid equilibrium data of n-hexane+CO$_2$ mixture at a temperature of $T = 313$ K. The corresponding parameter set (cf. Table 1) is found to provide a good representation of the fluid-phase equilibria at temperatures of $T = 353$ and 393 K for pressures removed from the critical point, whereas the critical point is overestimated by the theory as can be seen from Figure 18 a). The results of MD simulations performed at the given temperatures compare well with the theory. The same force-field parameters can be used to study the fluid-phase be-

13

haviour of other members of the n-alkane homologous series: an isothermal pressure-composition (Px) phase diagram for the long-chained n-pentadecane+CO_2 mixture is displayed in Figure 18 b). The change of the fluid-phase behaviour compared to that of the shorter-chain alkanes is evident with the appearance of the liquid-liquid equilibrium at low temperatures (here at $T \sim 292$ K). In the theoretical prediction, the liquid-liquid immiscibility persists at high pressures, whereas the experimental results indicate that a total miscibility is acheived for pressures above 20 MPa. The vapour-liquid equilibrium is correctly described with the SAFT-γ Mie EOS [31] using the parameters given in Table 1. At the temperatures above the critical point of pure CO_2, the fluid-phase equilibrium is accurately reproduced by the equation of state at low and intermediate pressures, the critical point of the mixture is however overestimated. MD simulations performed based on the same force field reproduce the theoretical and experimental results to high accuracy.

The change from type II behaviour for the short chain alkane to type III for the long chain alkanes is evident from the three-dimensional representation of the fluid-phase equilibria of mixtures of CO_2 with n-hexane and n-pentadecane in Figure 19 and the corresponding PT projection in Figure 20. The phase behaviour of the n-hexane+CO_2 mixture is qualitatively reproduced, displaying the continuous vapour-liquid critical line, which connects the critical points of the both components, and the liquid-liquid critical line, which merges with the three-phase line in UCEP. Quantitatively, the vapour-liquid critical line is overestimated compared to the experimental data [151]. By contrast, the discontinuous vapour-liquid critical line can be identified in the PT representation of the n-pentadecane+CO_2 mixture, illustrating type III behaviour. Starting from the critical point of n-pentadecane, the PT projection of the vapour-liquid critical line exhibits a maximum and then a minimum with decreasing temperature until it finally merges with the liquid-liquid critical line. Again, only qualitative agreement with experiment is achieved: the experimental data [151] indicate that the critical line is characterized by a maximum at a temperature of $T \sim 385$ K and a pressure of $P \sim 23$ MPa and a minimum at ~ 301 K and ~ 12 MPa, while the critical line predicted with the SAFT-γ Mie EOS has a maximum at ~ 450 K and ~ 35 MPa and a minimum at ~ 350 K and ~ 30 MPa.

An analysis of the behaviour of the density of the n-pentadecane+CO_2 mixture predicted with the SAFT-γ Mie EOS is also made by comparison with the corresponding experimental data at different temperatures and pressures. Mass barotropy has been observed experimentally for mixtures of CO_2 with n-alkane homologues that exhibit type III phase behaviour [152]. The shortest alkane that exhibits a barotropic density inversion in mixtures with CO_2 is n-tetradecane. The theoretical studies of Segura and co-workers [153, 154] have suggested that n-alkane+CO_2 mixtures characterized by type III behaviour exhibit both mass and molar barotropy, whereas type IV mixtures (e.g., n-tridecane+CO_2) only display molar barotropy. In our current work, the experimental densities reported for the n-pentadecane+CO_2 mixture by Tanaka *et al.* [155] at a temperature of $T = 313$ K are compared to the predictions of the SAFT-γ Mie EOS, thereby revealing excellent agreement (Figure 21). Further isotherms at temperatures of $T = 292$, 353, and 393 K are calculated with the EOS and are found to be in good correspondence with the results of MD simulation. Mass barotropy is observed at low temperatures: inversion is predicted at $T \sim 292$ K and $P \sim 9.5$ MPa, and at $T \sim 313$ K and $P \sim 22$ MPa with the EOS.

The adsorption phenomena in the interfacial region of the n-pentadecane+CO_2 mixture is studied at sub-critical ($T = 292$ K) and supercritical ($T = 353$ K) temperatures of CO_2 (cf. Figure 22). At these conditions, CO_2 is found to be adsorbed at the interface, whereas n-pentadecane does not exhibit any surface activity. The extraordinary surface adsorption of CO_2 in mixtures of long alkanes has already been examined in detail with a combination of the square-gradient theory and SAFT [156, 128]. At a pressure of $P = 5.2$ MPa, the maximum adsorption of the density profile at the temperature of $T = 292$ K is approximately three times higher than that observed at $T = 353$ K. The large excess adsorption exhibited at the lower temperatures is an indicator of the proximity to the liquid-liquid equilibrium (Figure 18). An increase in the density of CO_2 in both phases and in the interfacial region is observed with increasing pressure.
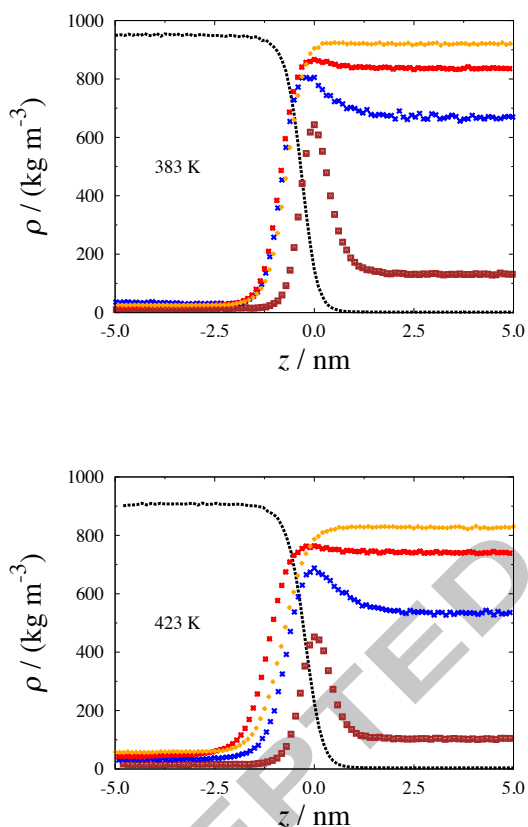
14

Figure 6: Density profiles at the interface of the carbon dioxide+water binary mixture at temperatures of T = 383 and 423 K and different pressures obtained with our SAFT-γ Mie CG force field by direct molecular-dynamics simulation using the parameters given in Table 1. The dotted black curves denote the density profiles for water at P = 8.18 MPa, and the symbols represent the density profiles for carbon dioxide at P = 8.18 (brown squares), 31.87 (blue crosses), 62.30 (red stars), and 102.10 MPa (yellow pluses).
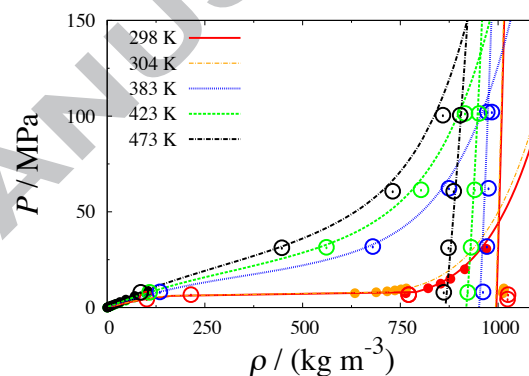
Figure 7: Isothermal pressure-density ($P\rho$) slices of the fluid-phase equilibria for the carbon dioxide+water binary mixture at temperatures of T = 298, 304, 383, 423, and 473 K. The filled circles correspond to experimental densities for the saturated phases [146]. The curves correspond to the predictions with the SAFT-γ Mie EOS [31] using the parameters given in Table 1, and the empty circles are the corresponding phase boundaries obtained with our SAFT-γ CG Mie force field by direct molecular-dynamics simulation.

15
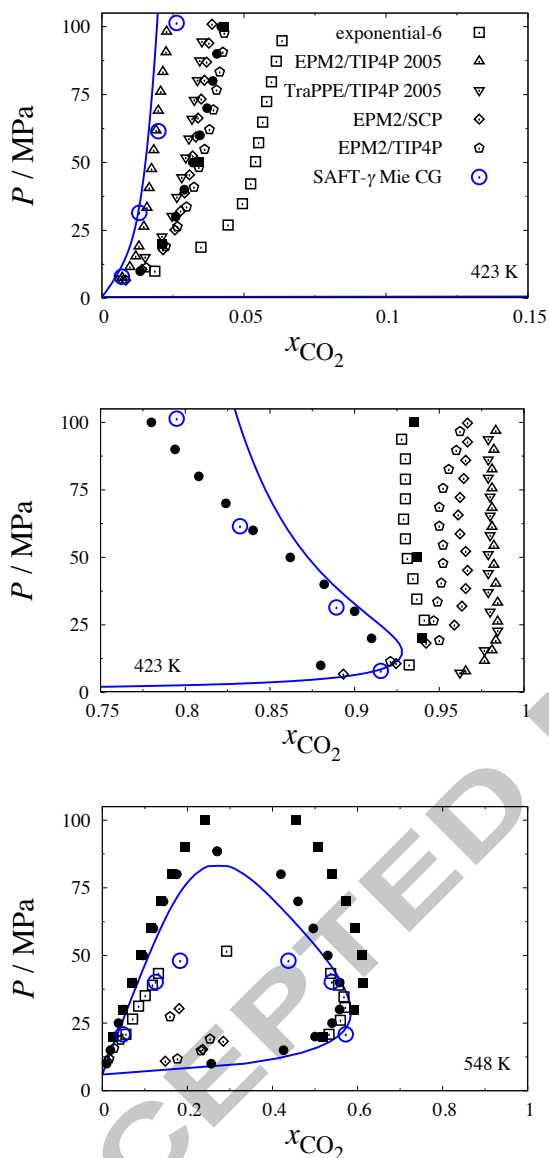
Figure 8: Isothermal pressure-composition (Px) slices of the fluid-phase equilibria for the carbon dioxide+water binary mixture at temperatures of T = 423 and 548 K. The filled symbols correspond to experimental data of Todheide and Franck [1] (■) and of Takenouchi and Kennedy [2] (●). The continuous blue curves corresponds to the predictions with the SAFT-γ Mie EOS [31] using the parameters given in Table 1, and the blue empty circles are the corresponding phase boundaries obtained with our SAFT-γ CG Mie force field by direct molecular-dynamics simulation. The results of the CG simulations are compared with the data obtained using some popular atomistic models as reported in reference [92]: exponential-6 (□); EPM2/TIP4P2005 (△); TraPPE/TIP4P2005 (▽); EPM2/SPC (◇); EPM2/TIP4P (⬠). The unlike-pair parameters of the atomistic force fields are based on the standard Lorentz-Berthelot combining rules.
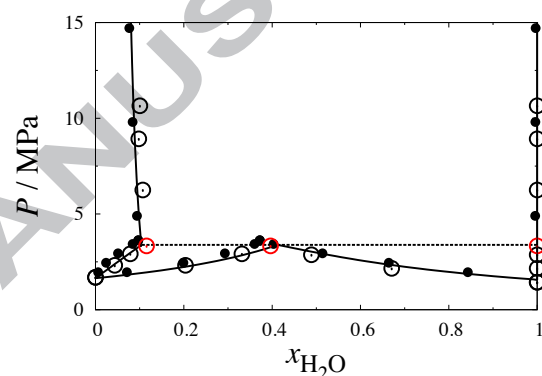
Figure 9: Isothermal pressure-composition (Px) slice of the fluid-phase equilibria for the n-hexane+water binary mixture at a temperature of T = 473 K. The filled circles correspond to the experimental vapour-liquid and liquid-liquid equilibrium data [147, 148, 149]. The continuous curves represent to the description with the SAFT-γ Mie EOS [31] using the parameters given in Table 1. The empty circles are the corresponding phase boundaries obtained with our SAFT-γ CG Mie force field by direct molecular-dynamics simulation: the heteroazeotropic point at a pressure of P = 3.33 MPa with composition $x_{H_2O}^{L_1} \sim 1.0$, $x_{H_2O}^G$ = 0.396, and $x_{H_2O}^{L_2}$ = 0.116 is highlighted in red.

16
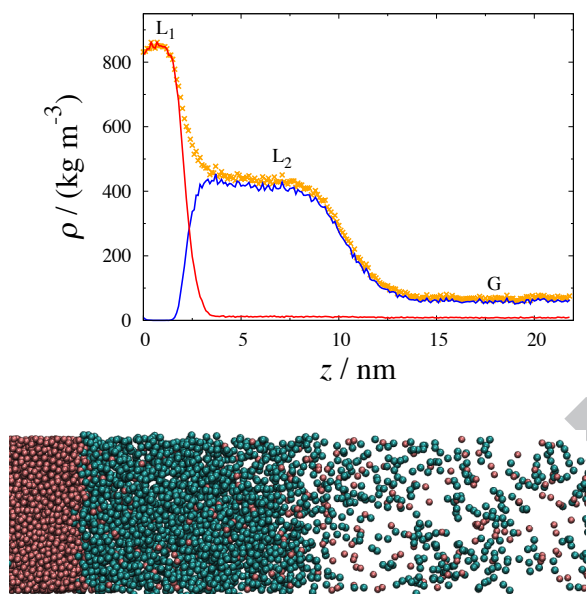
Figure 10: Total density profile (yellow crosses) of the *n*-hexane+water binary mixture at the three-phase co-existence (heteroazeotrope) corresponding to the temperature of $T = 473$ K and a pressure of $P = 3.33$ MPa obtained with our SAFT-γ Mie CG force field by direct molecular-dynamics simulation using the parameters given in Table 1. L_1 denotes the water-rich liquid phase, L_2 denotes *n*-hexane-rich liquid phase, G denotes the gas phase. The composition of the heteroazeotrope is $x_{H_2O}^{L_1} \sim 1.0$, $x_{H_2O}^{G} = 0.396$, and $x_{H_2O}^{L_2} = 0.116$. In the snapshot of a representative configuration during the simulation, the water molecules are displayed in red (red density profile in upper panel) and *n*-hexane in blue (blue density profile in upper panel).
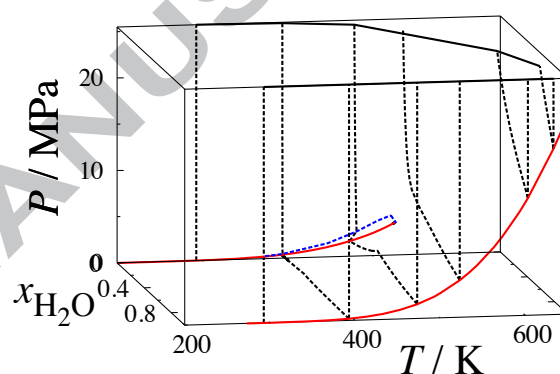
Figure 11: Three-dimensional pressure-temperature-composition (PTx) surface of the fluid-phase equilibria for the *n*-hexane+water binary mixture predicted with the SAFT-γ Mie EOS [31] using the parameters given in Table 1. The continuous red curves on the opposite faces of the prism represent the vapour pressures of the pure components, the dashed blue curves are the predictions for the critical line and the *PT* projection of the three-phase line, and the dashed black curves correspond to isothermal pressure-composition (Px) sections.
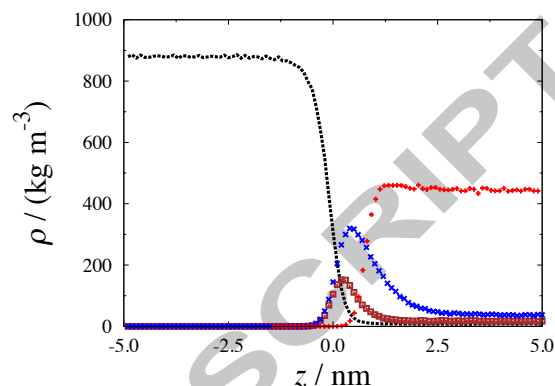
17

Figure 13: Density profiles at the interface of the *n*-hexane+water binary mixture at a temperature of $T = 473$ K and different pressures determined with our SAFT-γ Mie CG force field by direct molecular-dynamics simulation using the parameters given in Table 1. The dashed black curve denotes the density profile for water at $P = 2.16$ MPa, the symbols represent the density profiles for *n*-hexane at $P = 2.16$ (brown squares), 2.87 (blue crosses), and 6.25 MPa (red pluses).
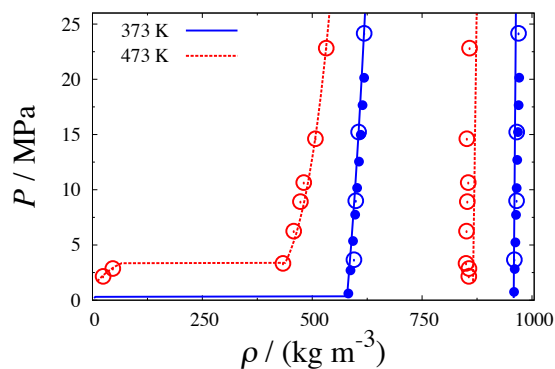

Figure 12: Pressure-temperature (*PT*) projection of the fluid-phase equilibria for the *n*-hexane+water binary mixture. The red circles correspond to the experimental vapour pressures of the pure components [138], and the blue circles correspond to the experimental vapour-liquid critical line and three-phase line [3]. The curves represent the calculations with the SAFT-γ Mie EOS [31] using the parameters given in Table 1: the continuous red curves are the vapour pressures of the pure components, and the dashed blue curves are the vapour-liquid critical line and three-phase line. An enlarged region close to the critical point of pure *n*-hexane is shown in the inset.

Figure 14: Isothermal pressure-density (*P*ρ) slices of the fluid-phase equilibria for the *n*-hexane+water binary mixture at $T = 373$ (blue/continuous) and 473 K (red/dashed). The filled circles correspond to experimental density data from Table 3. The curves represent the predictions with the SAFT-γ Mie [31] using the parameters given in Table 1, and the empty circles represent the corresponding phase boundaries obtained with our SAFT-γ CG Mie force field by direct MD simulation.
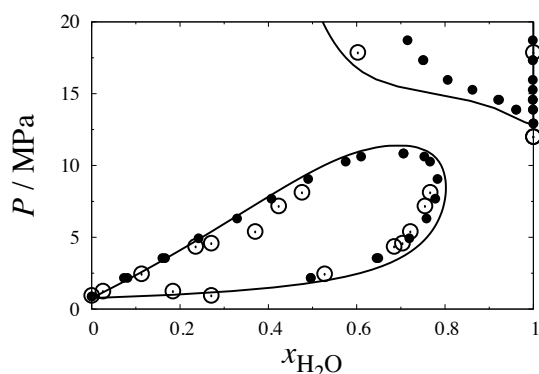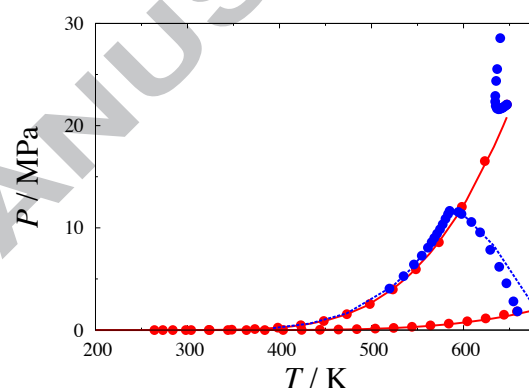
18

Figure 15: Isothermal pressure-composition (Px) slice of the fluid-phase equilibria for the n-dodecane+water binary mixture at a temperature of $T = 603$ K. The filled circles correspond to experimental vapour-liquid and liquid-liquid equilibrium data [4]. The continuous curves represent the predictions with SAFT-γ Mie EOS [31] using the parameters given in Table 1. The empty circles are the corresponding phase boundaries obtained with our SAFT-γ CG Mie force field by direct MD simulation.

Figure 17: Pressure-temperature (PT) projection of the fluid-phase equilibria for the n-dodecane+water binary mixture. The red circles correspond to the experimental vapour pressures of the pure components [138], and the blue circles correspond to the experimental vapour-liquid critical line and three-phase line [3]. The curves represent the predictions with the SAFT-γ Mie EOS [31] using the parameters given in Table 1: the continuous red curves are the vapour pressures of the pure components, and the dashed blue curves are the vapour-liquid critical line and three-phase line.
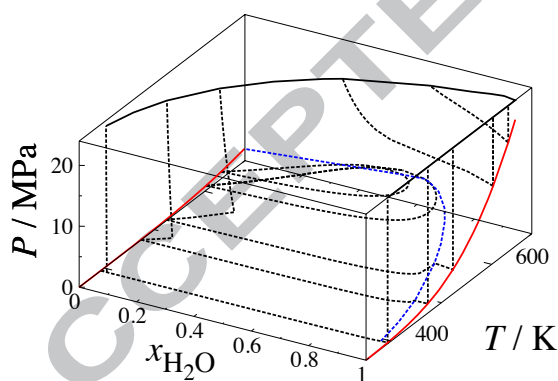

Figure 16: Three-dimensional pressure-temperature-composition (PTx) surface of the fluid-phase equilibria for the n-dodecane+water binary mixture predicted with the SAFT-γ Mie EOS [31] using the parameters given in Table 1. The continuous red curves on the opposite faces of the prism represent the vapour pressures of the pure components, the dashed blue curves are the predictions for the critical line and PT projection of the three-phase line, and the dashed black curves correspond to isothermal pressure-composition (Px) sections.
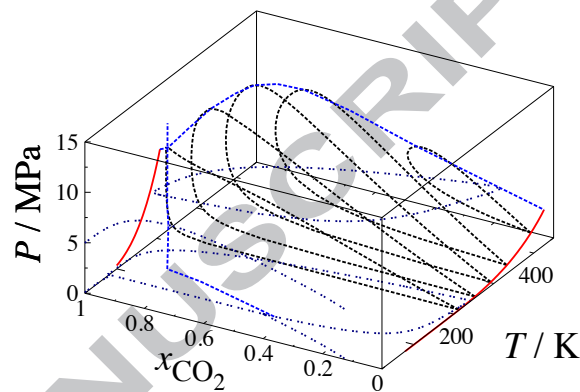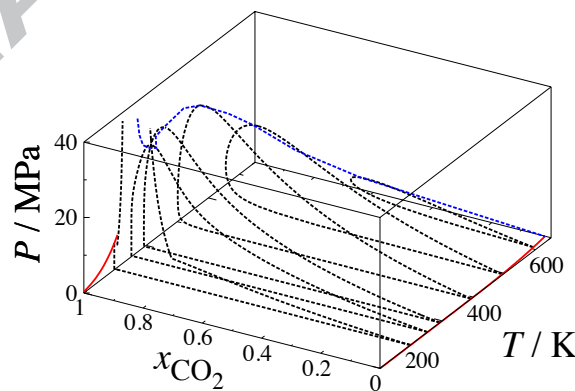
19

(a)

(b)
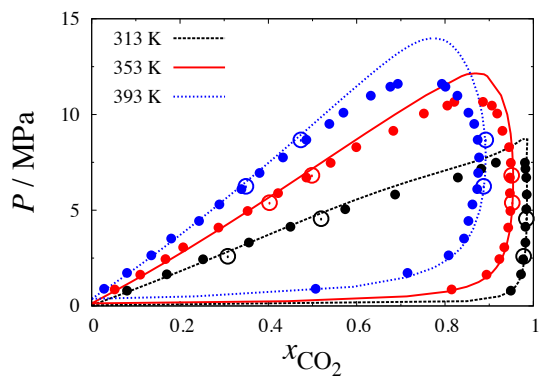
(a)
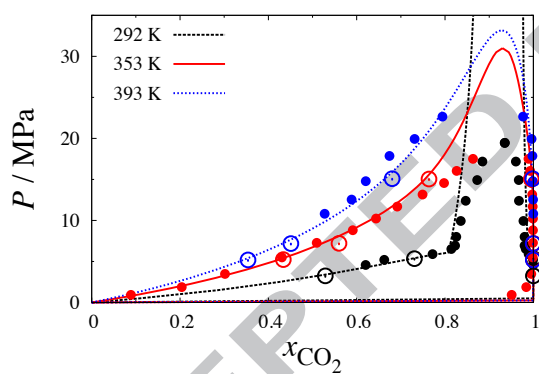
(b)

Figure 18: Isothermal pressure-composition (Px) slice of the fluid-phase equilibria of the (a) n-hexane+carbon dioxide and (b) n-pentadecane+carbon dioxide binary mixtures for isotherms corresponding to temperatures of T = 313, 353, 393 K and to T = 292, 353, 393 K, respectively. The filled circles are the experimental vapour-liquid and liquid-liquid equilibrium data [146]. The curves represent the description with the SAFT-γ Mie EOS [31] using the parameters given in Table 1. The empty circles are the corresponding fluid-phase boundaries obtained with our SAFT-γ CG Mie force field by direct MD simulation.
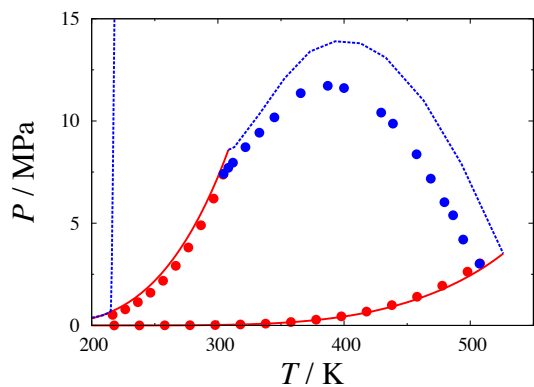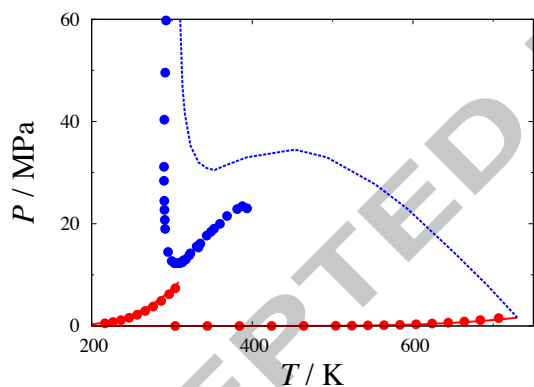
Figure 19: Three-dimensional pressure-temperature-composition (PTx) surface of the fluid-phase equilibria of the (a) n-hexane+carbon dioxide and (b) n-pentadecane+carbon dioxide binary mixtures predicted with the SAFT-γ Mie EOS [31] using the parameters given in Table 1. The continuous red curves on the opposite faces of the prism represent the vapour pressures of the pure components, the dashed blue curves are the critical lines and the PT projection of the three-phase line, and the dashed black curves correspond to isothermal pressure-composition (Px) sections.

20

(a)

(b)

Figure 20: Pressure-temperature (PT) projection of the fluid-phase equilibria of the (a) n-hexane+carbon dioxide and (b) n-pentadecane+carbon dioxide binary mixtures. The red circles correspond to the experimental vapour pressures of the pure components [138], and the blue circles correspond to the experimental vapour-liquid critical line [151]. The curves represent the description with the SAFT-γ Mie EOS [31] using the parameters given in Table 1: the continuous red curves are the vapour pressures of the pure components, and the dashed blue curves are the vapour-liquid critical line and three-phase line.
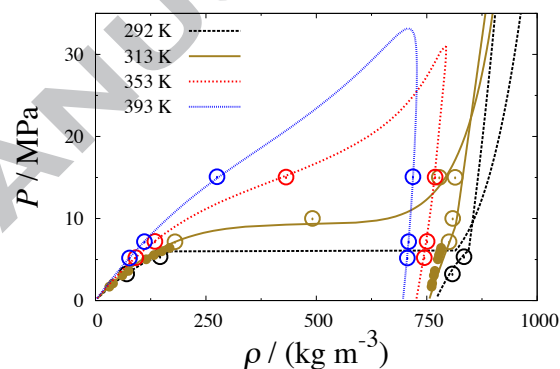

Figure 21: Isothermal pressure-density ($P\rho$) slices of the fluid-phase equilibria of the n-pentadecane+carbon dioxide binary mixture at temperatures of T = 292, 313, 353, and 393 K. The filled circles correspond to experimental density data for the saturated phases at T = 313 K [155]. The curves represent the description with the SAFT-γ Mie EOS [31] using the parameters given in Table 1. The empty circles are the corresponding fluid-phase boundaries obtained with our SAFT-γ CG Mie force field by direct MD simulation.
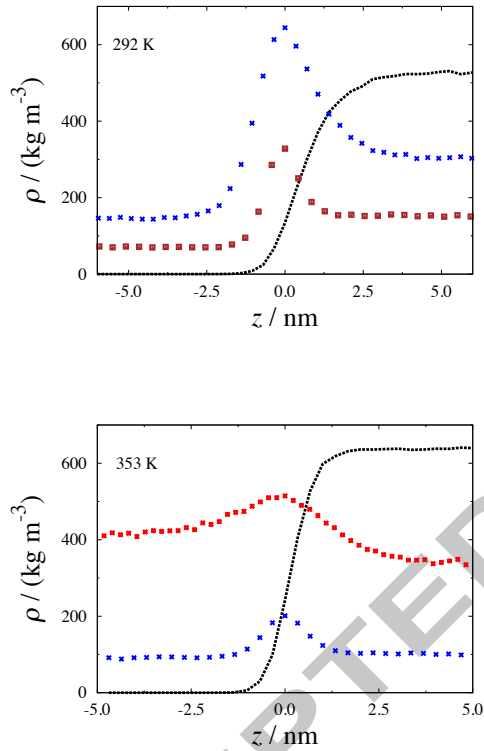
21

Figure 22: Density profiles at the interface of the *n*-pentadecane+carbon dioxide binary mixture at temperatures of $T = 292$ and 353 K and different pressures determined with our SAFT-γ Mie CG force field by direct molecular-dynamics simulation using the parameters given in Table 1. The dashed curve denotes the density profile of *n*-pentadecane at a pressure of $P = 5.2$ MPa, and the symbols represent the density profiles of carbon dioxide at $P = 3.2$ (brown squares), 5.2 (blue crosses), and 15.4 MPa (red stars).

22

3.4. n-decane+carbon dioxide+water ternary mixture

A recent and comprehensive experimental study of the n-decane+CO_2+H_2O ternary mixture has been undertaken by Forte *et al.* [157]. As the authors point out, a large part of the observable fluid-phase diagram is characterized by a three-phase region due to the immiscibility of the corresponding binary systems. In our current work, we compare the experimental data with the description obtained with the SAFT-γ Mie EOS and from MD simulations of the CG models. No additional parameters need to be determined for the ternary mixture, as all of the binary unlike interaction parameters have been specified for the binary systems.

In Table 4 and Figure 23 we compare the experimental [157] coexistence compositions of the ternary mixture with the predictions of the SAFT-γ Mie EOS and the MD simulations at T = 393 K and four different pressures removed from critical region (P = 6.02, 7.58, 9.59, and 11.81 MPa). The fluid-phase behaviour is clearly dominated by a region of three-phase equilibria, the extent of which decreases with increasing pressure. The SAFT-γ Mie EOS can be seen to provide an accurate description of the experimental measurements of the three-phase compositions for this range of thermodynamic conditions. Additionally the extent of the two-phase coexistence is well represented with the theory. Only very small single-phase regions can be detected at the margins of the ternary phase diagram. The compositions of the CO_2- and H_2O-rich phases obtained by MD simulation of the three-phase region with the corresponding SAFT-γ CG Mie force fields are in good agreement with theoretical predictions; the solubility of CO_2 in the n-alkane-rich phase is slightly overestimated for all pressures. The overall trend of increasing solubility with pressure can be correctly captured by simulations.

The density profiles of the n-decane+CO_2+H_2O ternary mixture at P = 6.02 MPa are displayed in Figure 24. Three phases (H_2O-rich phase L_1, n-decane-rich phase L_2, and CO_2-rich phase G) can clearly be distinguished from the magnitude of the total density, and are also apparent from the snapshot of the MD simulation. From the figure one finds that CO_2 exhibits a large adsorption peak at the interface between the H_2O-rich and n-decane-rich phases and a small adsorption peak at the interface between the CO_2-rich and n-decane-rich phases. The density and the width of the interfaces are also found to increase with increasing pressure.
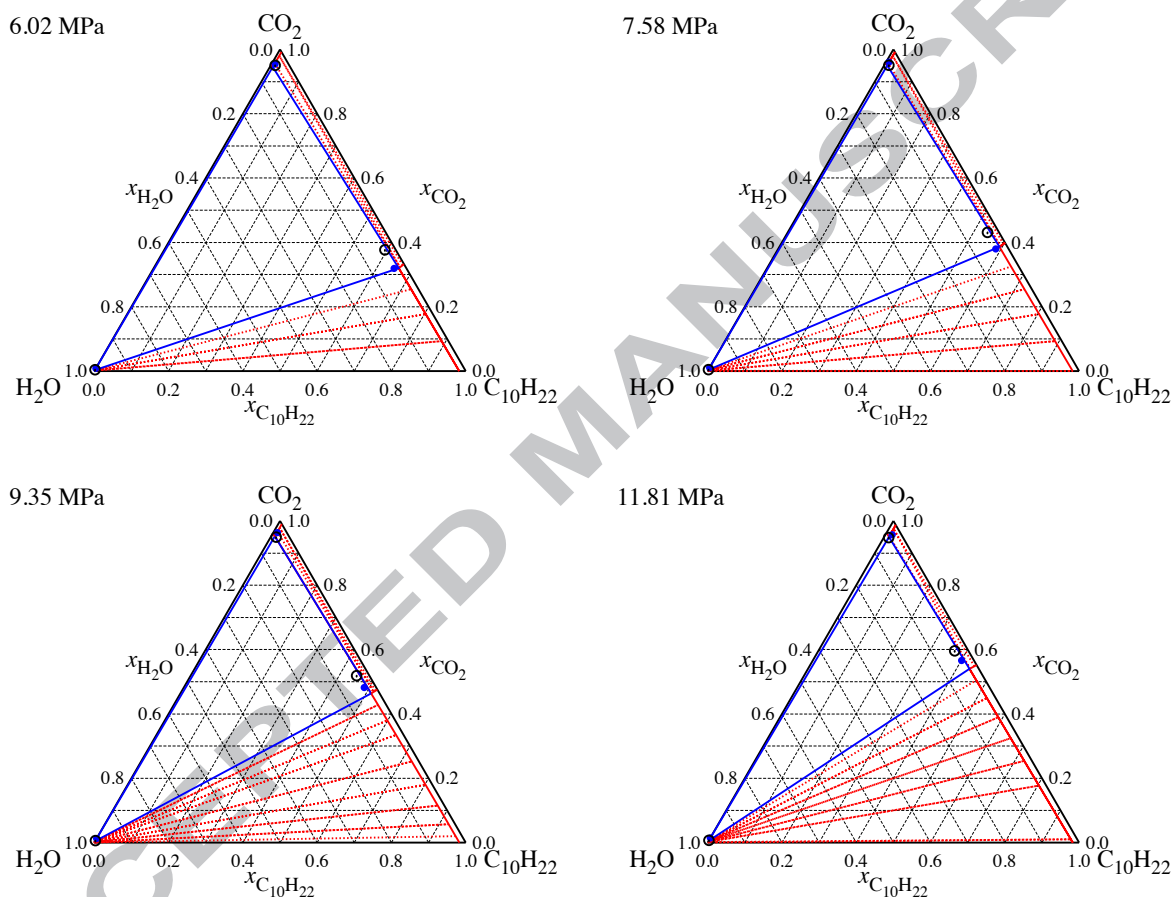
Figure 23: Ternary fluid-phase diagram for the *n*-decane+carbon dioxide+water mixture at $T = 393$ K and $P = 6.02$, 7.58, 9.35 and 11.81 MPa, respectively. The filled circles are the experimental values for the three-phase equilibrium region [157]; the continuous blue lines are SAFT-γ Mie [31] predictions of the three-phase equilibrium region, the dashed red lines are the corresponding two-phase coexistence tie-lines, and the continuous red curves the phase boundaries. The empty circles are the phase boundaries of the three-phase region determined with our SAFT-γ Mie CG force field by direct molecular-dynamics simulation using the parameters given in Table 1.

Table 4: Comparison of the experimental [157] fluid-equilibrium phase compositions with those predicted by the SAFT-γ Mie EOS [31] and obtained from the SAFT-gamma CG Mie force fields by direct MD simulations of the n-decane+carbon dioxide+water ternary mixture at a temperature of T = 393.15 K and different pressures.

		expt.			SAFT			MD		
P/ MPa	Phase	$x_{C_{10}H_{22}}^{expt}$	$x_{CO_2}^{expt}$	$x_{H_2O}^{expt}$	$x_{C_{10}H_{22}}^{SAFT}$	$x_{CO_2}^{SAFT}$	$x_{H_2O}^{SAFT}$	$x_{C_{10}H_{22}}^{MD}$	$x_{CO_2}^{MD}$	$x_{H_2O}^{MD}$
6.02	I	4.50×10^{-6}	0.0086	0.9914	0	0.0031	0.9969	0	0.0076	0.9924
	II	0.0097	0.9542	0.0361	0.0079	0.9454	0.0467	0.0137	0.9447	0.0416
	III	0.6477	0.3191	0.0332	0.6598	0.3197	0.0204	0.5932	0.3757	0.0311
7.58	I	2.70×10^{-6}	0.0107	0.9893	0	0.0038	0.9962	0	0.0074	0.9926
	II	0.0078	0.9605	0.0317	0.0084	0.9503	0.0413	0.0130	0.9473	0.0397
	III	0.5859	0.3795	0.0346	0.5924	0.3862	0.0214	0.4906	0.4751	0.0343
9.59	I	2.60×10^{-6}	0.0127	0.9873	0	0.0046	0.9954	0	0.0065	0.9935
	II	0.0112	0.9636	0.0252	0.0099	0.9522	0.0379	0.0142	0.9482	0.0377
	III	0.4857	0.4821	0.0322	0.5135	0.4636	0.0229	0.4077	0.5527	0.0396
11.81	I	8.30×10^{-7}	0.0145	0.9855	1.44×10^{-9}	0.0054	0.9946	0	0.0072	0.9928
	II	0.0184	0.9569	0.0247	0.0131	0.9500	0.0369	0.0134	0.9481	0.0386
	III	0.4006	0.566	0.0334	0.4349	0.5402	0.0250	0.3670	0.5961	0.0370

4. Conclusions

Figure 24: Total density profile (yellow crosses) of the ternary n-decane+carbon dioxide+water ternary mixture at $T = 393$ K and $P = 6.02$ MPa for a global composition of $x_{C_{10}H_{22}} = 0.1$, $x_{CO_2} = 0.5$ determined with our SAFT-γ Mie CG force field by direct molecular-dynamics simulation using the parameters given in Table 1. The water-rich liquid phase is denoted by L_1, n-decane-rich liquid phase by L_2, and the carbon dioxide-rich gas phase by G. In the snapshot of a representative configuration during the simulation, water molecules are displayed in red, n-decane in blue, and carbon dioxide in grey . In the snapshot of a representative configuration during the simulation, the water molecules are displayed in red (red density profile in upper panel), n-hexane in blue (blue density profile in upper panel), and carbon dioxide in black (black density profile in upper panel).

In our work we employ the SAFT-γ CG Mie force field to study binary and ternary mixtures comprising of water, carbon dioxide, and n-alkanes. Based on the models developed for pure components and binary-interaction parameters informed by the SAFT-γ Mie equation of state, we obtain a quantitative description of multicomponent, multiphase equilibria. The phase compositions, densities, critical lines, and three-phase lines predicted by the theory are found to accurately match the experimental data. In addition, the same intermolecular parameter set is employed directly in molecular-dynamics simulations, essentially reproducing the aforementioned results but also allowing the study of interfacial providing a microscopic molecular treatment of the system.

The key to the success of the SAFT-γ CG Mie procedure is that the EOS is based on a well defined Hamiltonian and thus can be used to extract the molecular force-field parameters directly from the macroscopic properties of the system. This top-down coarse-graining approach offers a direct link between the theory, simulation, and experiment, thereby allowing multiscale modelling of the system. An advantage of the theory over simulation or experiment is that it allows one to gain an overview over the entire phase diagram in a very efficient manner. On the other hand, molecular simulation provides microscopic information about the structural and interfacial properties, which are not directly accessible to the equation of state and difficult to probe experimentally.
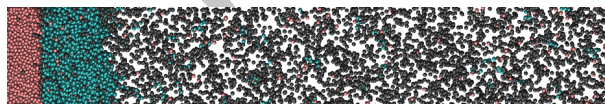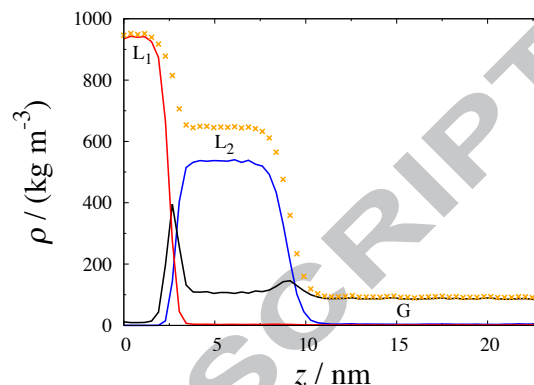
Appendix

Density measurements of the n-hexane+water mixture

The mass densities of the *n*-hexane+H_2O binary mixture are measured at a temperature of $T = 373.15$ K over the pressure range of $P = 0.6$ to 20 MPa by using a stainless steel high-pressure liquid-liquid equilibrium cell and a DMA HP densimeter (Anton Paar GmbH, Austria) with an accuracy of 5×10^{-3} kg m^{-3}. The experimental procedure for determining densities is as follows. First the densimeter is calibrated by using two reference fluids, ultra high purity nitrogen (UHP = 99.995%) and ultra-pure water. After degasification in an ultrasonic bath (model 1210, Branson, Inc.), approximately, 20 cm^3 of each pure fluid is introduced in the high-pressure cell. The chamber has two orifices (one at the top and the other at the bottom) and it is equipped with appropriately sealed borosilicate glass windows, which allow visualization of the inner space during operation. The cell is heated to the desired temperature by means of electric band heaters operated by a Watlow temperature controller model TC-211-K-989 (USA). The temperature of the sample in the vessel is measured by means of a K-type thermocouple, and maintained constant to within ±0.1 K. At the specified temperature, the mixture is well stirred with a magnetic stirrer for several hours (7 to 10 hr). The desired experimental pressure is then fixed by means a positive displacement pump (ELDEX HP, B- 100-S-2 CE, USA), and the experimental mixture is allowed to rest for at least 12 hr, in order to guarantee phase separation. After this equilibration step, each bulk phase (organic and aqueous) is transported to the high-pressure densimeter through a heated stainless steel tube. The determination of the mass density is based on measuring the period of oscillation of a vibrating U-shaped tube filled with the fluid mixture sample. During the operation, the temperature of the apparatus is maintained constant to within ±0.01 K. The pressure is measured by means a Swagelok type S pressure transducer connected to the densimeter. The density measurements are repeated 25 times for each thermodynamic condition, and the average reported.

Purity of Materials

n-hexane and ultra pure H_2O purchased from Merck, are used without further purification. The purity and source of the components is reported in Table .5 as determined by gas chromatography (GC). The mass density (ρ) of the pure fluids at a temperature of $T = 298.15$ K and atmospheric pressure are reported in Table .6. The reported values are also compared with those previously reported in the NIST-REFPROP [158] database.

Table .5: Source and Gas chromatography (GC) purities (mass fraction) of pure fluids used without purification.

Component	Source	mass fraction by GC
n-hexane	Merck	0.996
ultra pure water	Merck	—

Table .6: The liquid mass density (ρ) of the pure fluids at 298.15 K and 101.3 kPa. The standard uncertainties of the measurments are: $\rho \pm 0.4$ kg m^{-3}; $T \pm 0.1$ K, $P \pm 0.3$ kPa.

| Component (purity / mass fraction)	ρ / (kg m^{-3})	
	Expt.	Lit. [158]
n-hexane	655.19	656.03
ultra pure water	996.70	997.07

References

[1] K. Todheide and E. U. Franck, *Zeitschrift fuer Physikalische Chemie Neue Folge*, 1963, **37**, 387–401.

[2] S. Takenouchi and J. Kennedy, *American Journal of Science*, 1964, **262**, 1055–1074.

[3] E. Brunner, *Journal of Chemical Thermodynamics*, 1990, **22**, 335–353.

[4] R. L. Stevenson, D. S. Labracio, T. A. Beaton and M. C. Thies, *Fluid Phase Equilibria*, 1994, **93**, 317–336.

[5] R. L. Scott and P. H. Van Konynenburg, *Discussions of the Faraday Society*, 1970, **49**, 87–97.

[6] P. H. van Konynenburg and R. L. Scott, *Philosophical Transactions of the Royal Society of London*, 1980, **298**, 495.

[7] G. Schneider, Z. Alwani, W. Heim, E. Horvath and E. U. Franck, *Chemie Ingenieur Technik*, 1967, **39**, 649.

[8] G. M. Schneider, *Advances in Physical Chemistry*, 1970, **17**, 1.

[9] L. W. Diamond and N. N. Akinfiev, *Fluid Phase Equilibria*, 2003, **208**, 265–290.

[10] N. Spycher, K. Pruess and J. Ennis-King, *Geochimica Et Cosmochimica Acta*, 2003, **67**, 3015–3031.

[11] G. M. Kontogeorgis and G. K. Folas, *Thermodynamic Models for Industrial Applications: From Classical and Advanced Mixing Rules to Association Theories*, John Wiley and Sons Ltd, West Sussex, United Kingdom, 2010.

[12] M. Cismondi, S. B. Rodriguez-Reartes, J. M. Milanesio and M. S. Zabaloy, *Industrial & Engineering Chemistry Research*, 2012, **51**, 6232–6250.

[13] W. G. Chapman, K. E. Gubbins, G. Jackson and M. Radosz, *Fluid Phase Equilibria*, 1989, **52**, 31–38.

[14] W. G. Chapman, K. E. Gubbins, G. Jackson and M. Radosz, *Industrial & Engineering Chemistry Research*, 1990, **29**, 1709–1721.

[15] M. S. Wertheim, *Journal of Statistical Physics*, 1984, **35**, 19–34.

[16] M. S. Wertheim, *Journal of Statistical Physics*, 1984, **35**, 35–47.

[17] M. S. Wertheim, *Journal of Statistical Physics*, 1986, **42**, 459–476.

[18] M. S. Wertheim, *Journal of Statistical Physics*, 1986, **42**, 477–492.

[19] G. Jackson, W. G. Chapman and K. E. Gubbins, *Molecular Physics*, 1988, **65**, 1–31.

[20] W. G. Chapman, G. Jackson and K. E. Gubbins, *Molecular Physics*, 1988, **65**, 1057–1079.

[21] A. Gil-Villegas, A. Galindo, P. J. Whitehead, S. J. Mills, G. Jackson and A. N. Burgess, *Journal of Chemical Physics*, 1997, **106**, 4168–4186.

[22] L. Davies, A. Gil-Villegas and G. Jackson, *International Journal of Thermophysics*, 1998, **19**, 675–686.

[23] T. Lafitte, D. Bessieres, M. M. Pineiro and J. L. Daridon, *Journal of Chemical Physics*, 2006, **124**, 024509.

[24] T. Lafitte, A. Apostolakou, C. Avendaño, A. Galindo, C. S. Adjiman, E. A. Müller and G. Jackson, *Journal of Chemical Physics*, 2013, **139**, 154504.

[25] F. J. Blas and L. F. Vega, *Journal of Chemical Physics*, 1998, **109**, 7405–7413.

[26] J. Gross and G. Sadowski, *Industrial & Engineering Chemistry Research*, 2001, **40**, 1244–1260.

[27] S. Tamouza, J. P. Passarello, P. Tobaly and J.-C. de Hemptinne, *Fluid Phase Equilibria*, 2004, **222**, 67–76.

[28] S. Tamouza, J. P. Passarello, P. Tobaly and J.-C. de Hemptinne, *Fluid Phase Equilibria*, 2005, **228**, 409–419.

[29] A. Lymperiadis, C. S. Adjiman, A. Galindo and G. Jackson, *Journal of Chemical Physics*, 2007, **127**, 234903.

[30] A. Lymperiadis, C. S. Adjiman, G. Jackson and A. Galindo, *Fluid Phase Equilibria*, 2008, **274**, 85–104.

[31] V. Papaioannou, T. Lafitte, C. Avendano, C. S. Adjiman, G. Jackson, E. A. Müller and A. Galindo, *Journal of Chemical Physics*, 2014, **140**, 054107.

[32] Y. Peng, K. D. Goff, M. C. dos Ramos and C. McCabe, *Fluid Phase Equilibria*, 2009, **277**, 131–144.

[33] G. M. Kontogeorgis, E. C. Voutsas, I. V. Yakoumis and D. P. Tassios, *Industrial & Engineering Chemistry Research*, 1996, **35**, 4310–4318.

[34] A. Galindo and F. J. Blas, *Journal of Physical Chemistry B*, 2002, **106**, 4503–4515.

[35] F. J. Blas and A. Galindo, *Fluid Phase Equilibria*, 2002, **194**, 501–509.

[36] J. Garcia, L. Lugo and J. Fernandez, *Industrial & Engineering Chemistry Research*, 2004, **43**, 8345–8353.

[37] A. Valtz, A. Chapoy, C. Coquelet, P. Paricaud and D. Richon, *Fluid Phase Equilibria*, 2004, **226**, 333–344.

[38] J. Gross, *AIChE Journal*, 2005, **51**, 2556–2568.

[39] F. Llovell and L. F. Vega, *Journal of Physical Chemistry B*, 2006, **110**, 1350–1362.

[40] M. C. dos Ramos, F. J. Blas and A. Galindo, *Journal of Physical Chemistry C*, 2007, **111**, 15924–15934.

[41] M. C. dos Ramos, F. J. Blas and A. Galindo, *Fluid Phase Equilibria*, 2007, **261**, 359–365.

[42] N. Mac Dowell, F. Llovell, C. S. Adjiman, G. Jackson and A. Galindo, *Industrial & Engineering Chemistry Research*, 2010, **49**, 1883–1899.

[43] N. Mac Dowell, F. E. Pereira, F. Llovell, F. J. Bias, C. S. Adjiman, G. Jackson and A. Galindo, *Journal of Physical Chemistry B*, 2011, **115**, 8155–8168.

[44] E. Forte, *PhD Thesis*, Imperial College London, 2011.

[45] G. Niño Amézquita, D. van Putten and S. Enders, *Fluid Phase Equilibria*, 2012, **332**, 40–47.

[46] S. Dufal, T. Lafitte, A. J. Haslam, A. Galindo, G. N. I. Clark, C. Vega and G. Jackson, *Molecular Physics*, 2015, **113**, 948–984.

[47] B. H. Patel, P. Paricaud, A. Galindo and G. C. Maitland, *Industrial & Engineering Chemistry Research*, 2003, **42**, 3809–3823.

[48] L. F. Vega, F. Llovell and F. J. Blas, *Journal of Physical Chemistry B*, 2009, **113**, 7621–7630.

[49] A. Galindo, P. J. Whitehead, G. Jackson and A. N. Burgess, *Journal of Physical Chemistry*, 1996, **100**, 6781–6792.

[50] I. V. Yakoumis, G. M. Kontogeorgis, E. C. Voutsas, E. M. Hendriks and D. P. Tassios, *Industrial & Engineering Chemistry Research*, 1998, **37**, 4175–4182.

[51] E. C. Voutsas, G. C. Boulougouris, I. G. Economou and D. P. Tassios, *Industrial & Engineering Chemistry Research*, 2000, **39**, 797–804.

[52] X. S. Li and P. Englezos, *Fluid Phase Equilibria*, 2004, **224**, 111–118.

[53] M. B. Oliveira, J. A. P. Coutinho and A. J. Queimada, *Fluid Phase Equilibria*, 2007, **258**, 58–66.

[54] D. Nguyen-Huynh, J.-C. de Hemptinne, R. Lugo, J. P. Passarello and P. Tobaly, *Industrial & Engineering Chemistry*, 2011, **50**, 7457–7483.

[55] C. P. Emborsky, K. R. Cox and W. G. Chapman, *Industrial & Engineering Chemistry Research*, 2011, **50**, 7791–7799.

[56] V. Papaioannou, C. S. Adjiman, G. Jackson and A. Galindo, *Fluid Phase Equilibria*, 2011, **306**, 82–96.

[57] W. A. Fouad, D. Ballal, K. R. Cox and W. G. Chapman, *Journal of Chemical and Engineering Data*, 2013, **59**, 1016–1023.

[58] G. M. Kontogeorgis, M. L. Michelsen, G. K. Folas, S. Derawi, N. von Solms and E. H. Stenby, *Industrial & Engineering Chemistry Research*, 2006, **45**, 4869–4878.

[59] E. A. Müller and K. E. Gubbins, *Industrial & Engineering Chemistry Research*, 1995, **34**, 3662–3673.

[60] T. Kraska and K. E. Gubbins, *Industrial & Engineering Chemistry*, 1996, **35**, 47274737.

[61] T. Kraska and K. E. Gubbins, *Industrial & Engineering Chemistry*, 1996, **35**, 47384746.

[62] H. Zhao, Y. Ding and C. McCabe, *Journal of Chemical Physics*, 2007, **127**, 084514.

[63] X. Tang and J. Gross, *Fluid Phase Equilibria*, 2010, **293**, 11–21.

[64] R. Sun and J. Dubessy, *Geochimica et Cosmochimica Acta*, 2010, **74**, 19821998.

[65] P. Ungerer, B. Tavitian and A. Boutin, *Applications of Molecular Simulation in the Oil and Gas Industry: Monte Carlo Methods*, Editions Technip, 2005.

[66] P. Ungerer, C. Nieto-Draghi, V. Lachet, A. Wender, A. Di Lella, A. Boutin, B. Rousseau and A. H. Fuchs, *Molecular Simulation*, 2007, **33**, 287–304.

[67] M. P. Allen and D. J. Tildesley, *Computer Simulation of Liquids*, Oxford University Press, Oxford, 1987.

[68] McIntosh-Smith, D. Tchertanov, D. Nerukh, Stone, D. Baaden, D. Hayward, D. Glowacki, P. Olson, D. Zoppe, D. Petrov, D. Woods, Hall, D. Reiher, D. Brancale, Haag, D. O'Donoghue, D. Raffin, Iakovou, D. Raffin, D. Chavent, D. Montes, McIntosh-Smith, Thomas and P. Hirst, *Faraday Discussions*, 2014, **169**, 379–401.

[69] J. C. Palmer and P. G. Debenedetti, *AIChE Journal*, 2015, **61**, 370–383.

[70] S. T. Cui, H. D. Cochran and P. T. Cummings, *Journal of Physical Chemistry B*, 1999, **103**, 4485–4491.

[71] J. G. Harris and K. H. Yung, *Journal of Physical Chemistry*, 1995, **99**, 12021–12024.

[72] J. I. Siepmann, S. Karaborni and B. Smit, *Nature*, 1993, **365**, 330–332.

[73] P. Virnau, M. Müller, L. G. MacDowell and K. Binder, *Journal of Chemical Physics*, 2004, **121**, 2169–2179.

[74] J. J. Potoff, J. R. Errington and A. Z. Panagiotopoulos, *Molecular Physics*, 1999, **97**, 1073–1083.

[75] J. Vorholz, V. I. Harismiadis, B. Rumpf, A. Z. Panagiotopoulos and G. Maurer, *Fluid Phase Equilibria*, 2000, **170**, 203234.

[76] H. Berendsen, J. Postma, W. van Gunsteren and J. Hermans, *Interaction Models for Water in Relation to Protein Hydration*,

28

(Reidel, Dordrecht, Netherlands, 1981, vol. 14, pp. 331–342.

[77] H. J. C. Berendsen, J. R. Grigera and T. P. Straatsma, *Journal of Physical Chemistry*, 1987, **91**, 6269–6271.

[78] W. L. Jorgensen, J. Chandrasekhar, J. D. Madura, R. W. Impey and M. L. Klein, *Journal of Chemical Physics*, 1983, **79**, 926–935.

[79] A. J. Haslam, A. Galindo and G. Jackson, *Fluid Phase Equilibria*, 2008, **266**, 105–128.

[80] L. Vlcek, A. A. Chialvo and D. R. Cole, *Journal of Physical Chemistry B*, 2011, **115**, 87758784.

[81] J. J. Potoff and J. I. Siepmann, *AIChE Journal*, 2001, **47**, 1676–1682.

[82] J. Vrabec, J. Stoll and H. Hasse, *Molecular Simulation*, 2005, **31**, 215–221.

[83] J. Vrabec, Y. L. Huang and H. Hasse, *Fluid Phase Equilibria*, 2009, **279**, 120–135.

[84] E. Johansson, K. Bolton, D. N. Theodorou and P. Ahlstrom, *Journal of Chemical Physics*, 2007, **126**, 224902.

[85] M. G. Martin and J. I. Siepmann, *Journal of Physical Chemistry B*, 1998, **102**, 2569–2577.

[86] D. Ballal, P. Venkataraman, W. A. Fouad, K. R. Cox and W. G. Chapman, *Journal of Chemical Physics*, 2014, **141**, 064905.

[87] J. R. Errington, G. C. Boulougouris, I. G. Economou, A. Z. Panagiotopoulos and D. N. Theodorou, *Journal of Physical Chemistry B*, 1998, **102**, 88658873.

[88] G. C. Boulougouris, J. R. Errington, I. G. Economou, A. Z. Panagiotopoulos and D. N. Theodorou, *Journal of Physical Chemistry B*, 2000, **104**, 49584963.

[89] I. G. Economou, *Fluid Phase Equilibria*, 2001, **183**, 259269.

[90] E. M. Yezdimer, A. A. Chialvo and P. T. Cummings, *Fluid Phase Equilibria*, 2001, **183**, 289294.

[91] A. L. Ferguson, P. G. Debenedetti and A. Z. Panagiotopoulos, *Journal of Physical Chemistry B*, 2009, **113**, 6405–6414.

[92] Y. Liu, A. Z. Panagiotopoulos and P. G. Debenedetti, *Journal of Physical Chemistry B*, 2011, **115**, 6629–6635.

[93] G. A. Orozco, I. G. Economou and A. Z. Panagiotopoulos, *Journal of Physical Chemistry B*, 2014, **118**, 11504–11511.

[94] O. A. Moultos, I. N. Tsimpanogiannis, A. Z. Panagiotopoulos and I. G. Economou, *Journal of Physical Chemistry B*, 2014, **118**, 55325541.

[95] O. A. Moultos, G. A. Orozco, I. N. Tsimpanogiannis, A. Z. Panagiotopoulos and I. G. Economou, *Molecular Physics*, 2015, **DOI**, 10.1080/00268976.2015.1023224.

[96] D. Reith, M. Putz and F. Muller-Plathe, *Journal of Computational Chemistry*, 2003, **24**, 1624–1636.

[97] G. A. Voth and S. Izvekov, *Journal of Physical Chemistry B*, 2005, **109**, 2469–2473.

[98] W. G. Noid, J. W. Chu, G. S. Ayton, V. Krishna, S. Izvekov, G. A. Voth, A. Das and H. C. Andersen, *Journal of Chemical Physics*, 2008, **128**, 244114.

[99] A. P. Lyubartsev and A. Laaksonen, *Physical Review E*, 1995, **52**, 3730–3737.

[100] E. A. Müller and G. Jackson, *Annual Review of Chemical and Biomolecular Engineering*, 2014, **5**, 405–427.

[101] A. Lofti, J. Vrabec and J. Fischer, *Molecular Physics*, 1992, **76**, 1319–1333.

[102] J. Vrabec, J. Stoll and H. Hasse, *Journal of Physical Chemistry B*, 2001, **105**, 12126–12133.

[103] J. Stoll, J. Vrabec and H. Hasse, *Fluid Phase Equilibria*, 2003, **209**, 29–53.

[104] R. W. Zwanzig, *Journal of Chemical Physics*, 1954, **22**, 1420–1426.

[105] J. A. Barker and D. Henderson, *Journal of Chemical Physics*, 1967, **47**, 4714–21.

[106] J. A. Barker and D. Henderson, *Reviews of Modern Physics*, 1976, **48**, 587–671.

[107] J. Y. Cui and J. R. Elliott, *Journal of Chemical Physics*, 2002, **116**, 8625–8631.

[108] J. R. Elliott, *Fluid Phase Equilibria*, 2002, **194**, 161–168.

[109] O. Unlu, N. H. Gray, Z. N. Gerek and J. R. Elliott, *Industrial & Engineering Chemistry Research*, 2004, **43**, 1788–1793.

[110] A. Vahid and J. R. Elliott, *AIChE Journal*, 2010, **56**, 485–505.

[111] A. F. Ghobadi and J. R. Elliott, *Fluid Phase Equilibria*, 2011, **306**, 5766.

[112] A. F. Ghobadi and J. R. Elliott, *Journal of Chemical Physics*, 2013, **139**, 234104.

[113] A. F. Ghobadi and J. R. Elliott, *Journal of Chemical Physics*, 2014, **141**, 024708.

[114] T. van Westen, T. J. H. Vlugt and J. Gross, *Journal of Physical Chemistry B*, 2011, **115**, 7872–7880.

[115] A. Hemmen and J. Gross, *Journal of Physical Chemistry B*, 2015, DOI: 10.1021/acs.jpcb.5b01354.

[116] A. Hemmen, A. Z. Panagiotopoulos and J. Gross, *Journal of Physical Chemistry B*, 2015, **119**, 70877099.

[117] C. Avendaño, T. Lafitte, A. Galindo, C. S. Adjiman, G. Jackson and E. A. Müller, *Journal of Physical Chemistry B*, 2011, **115**, 11154–11169.

[118] C. Avendaño, T. Lafitte, C. S. Adjiman, A. Galindo, E. A. Müller and G. Jackson, *Journal of Physical Chemistry B*, 2013, **117**, 2717–2733.

[119] S. Rahman, O. Lobanova, C. Braga, V. Raptis, E. A. Müller, G. Jackson and A. Galindo, *Journal of Physical Chemistry B*, 2015, submitted.

[120] T. Lafitte, C. Avendaño, V. Papaioannou, A. Galindo, C. S. Adjiman, G. Jackson and E. A. Müller, *Molecular Physics*, 2012, **110**, 1189–1203.

[121] O. Lobanova, C. Avendaño, T. Lafitte, E. A. Müller and G. Jackson, *Molecular Physics*, 2015, **113**, 1228–1249.

[122] O. Lobanova, C. Herdes, G. Jackson and E. A. Müller, *Soft Matter*, 2015, submitted.

[123] C. Herdes, E. E. Santiso, C. James, J. Eastoe and E. A. Müller, *Journal of Colloid and Interface Science*, 2015, **445**, 16–23.

[124] P. E. Theodorakis, E. A. Müller, R. V. Craster and O. K. Matar, *Langmuir*, 2015, **31**, 2304–2309.

[125] A. Mejia, C. Herdes and E. A. Müller, *Industrial & Engineering Chemistry Research*, 2014, **53**, 4131–4141.

[126] C. G. Aimoli, E. J. Maginn and C. R. A. Abreu, *Journal of Chemical & Engineering Data*, 2014, **59**, 3041–3054.

[127] C. G. Aimoli, E. J. Maginn and C. R. A. Abreu, *Journal of Chemical Physics*, 2014, **141**, 134101.

[128] A. Mejia, M. Cartes, H. Segura and E. A. Müller, *Journal of Chemical and Engineering Data*, 2014, **59**, 2928–2941.

[129] J. M. Míguez, J. M. Garrido, F. J. Blas, H. Segura, A. Mejía and M. M. Piñeiro, *J. Phys. Chem. C*, 2014, **118**, 24504–24519.

[130] C. Herdes, T. S. Totton and E. A. Müller, *Fluid Phase Equilibria*, 2015, DOI:10.1016/j.fluid.2015.07.014.

[131] C. G. Aimoli, E. J. Maginn and C. R. A. Abreu, *Fluid Phase Equilibria*, 2014, **368**, 80–90.

[132] N. Ramrattan, C. Avendaño, E. A. Müller and A. Galindo, *Molecular Physics*, 2015, **113**, 932–947.

[133] M. S. Wertheim, *Journal of Chemical Physics*, 1987, **87**, 73237331.

[134] F. Martinez-Veracoechea and E. A. Müller, *Molecular Simulation*, 2005, **31**, 33–43.

[135] W. G. Hoover, *Physical Review A*, 1985, **31**, 1695–1697.

[136] S. Nose, *Journal of Chemical Physics*, 1984, **81**, 511–519.

[137] D. van der Spoel, E. Lindahl, B. Hess, G. Groenhof, A. E. Mark and H. J. C. Berendsen, *Journal of Computational Chemistry*, 2005, **26**, 1701–1718.

[138] *Thermophysical Properties of Fluid Systems in NIST Chem-*

istry WebBook, NIST Standard Reference Database, Number 69; National Institute of Standards and Technology, Gaithersburg MD, http://webbook.nist.gov.

[139] R. W. Wiebe and V. L. Gaddy, *Journal of the American Chemical Society*, 1940, **62**, 815–817.

[140] R. W. Wiebe and V. L. Gaddy, *Journal of the American Chemical Society*, 1941, **63**, 475–477.

[141] M. B. King, A. Mubarak, J. D. Kim and T. R. Bott, *Journal of Supercritical Fluids*, 1992, **5**, 296–302.

[142] C. R. Coan and A. D. King, *Journal of the American Chemical Society*, 1971, **93**, 1857.

[143] K. Y. Song and R. Kobayashi, *SPE Formation Evaluation*, 1987, **2**, 500–508.

[144] P. C. Gillepsie and G. M. Wilson, *Gas Processors Association*, 1982, **Tulsa**, Research Report RR–48.

[145] E. A. Müller and A. Mejía, *Journal of Physical Chemistry Letters*, 2014, **5**, 1267–1271.

[146] *DETHERM Gesellschaft für Chemische Technik und Biotechnologie e.V.*, https://cdsdt.dl.ac.uk/detherm.

[147] A. Namiot, V. Skripka and Y. Lotter, *Deposited Doc. VINITI*, 1976, **76**, 1213.

[148] R. G. Sultanov and V. G. Skripka, *Deposited Doc. VINITI*, 1972, **72**, 4386.

[149] R. G. Sultanov and V. G. Skripka, *Deposited Doc. VINITI*, 1973, **73**, 5347.

[150] J. Rowlinson and F. Swinton, *Liquids and liquid mixtures*, Butterworth Scientific, 1982.

[151] J. G. Liu, Z. F. Qin, G. F. Wang, X. L. Hou and J. G. Wang, *Journal of Chemical and Engineering Data*, 2003, **48**, 1610–1613.

[152] J. van der Steen, T. W. Deloos and J. D. Arons, *Fluid Phase Equilibria*, 1989, **51**, 353–367.

[153] M. E. Flores, M. J. Tardon, C. Bidart, A. Mejia and H. Segura, *Fluid Phase Equilibria*, 2012, **313**, 171–181.

[154] M. J. Tardon, J. M. Garrido, H. Quinteros-Lama, A. Mejia and H. Segura, *Fluid Phase Equilibria*, 2012, **336**, 84–97.

[155] H. Tanaka, Y. Yamaki and M. Kato, *Journal of Chemical and Engineering Data*, 1993, **38**, 386–388.

[156] E. A. Müller and A. Mejia, *Fluid Phase Equilibria*, 2009, **282**, 68–81.

[157] E. Forte, A. Galindo and J. P. M. Trusler, *Journal of Physical Chemistry B*, 2011, **115**, 14591–14609.

[158] E. W. Lemmon, M. L. Huber and M. O. McLinden, *Reference Fluid Thermodynamic and Transport Properties-REFPROP*, 2013, version 9.1.

30
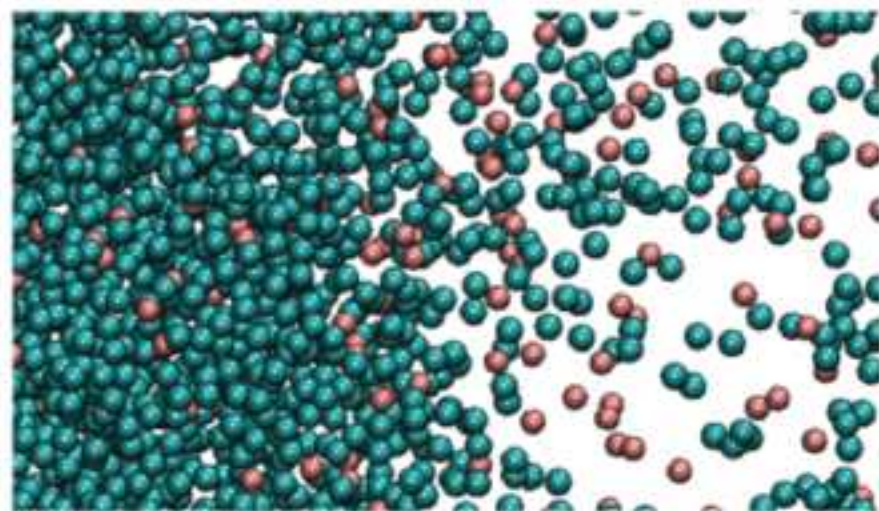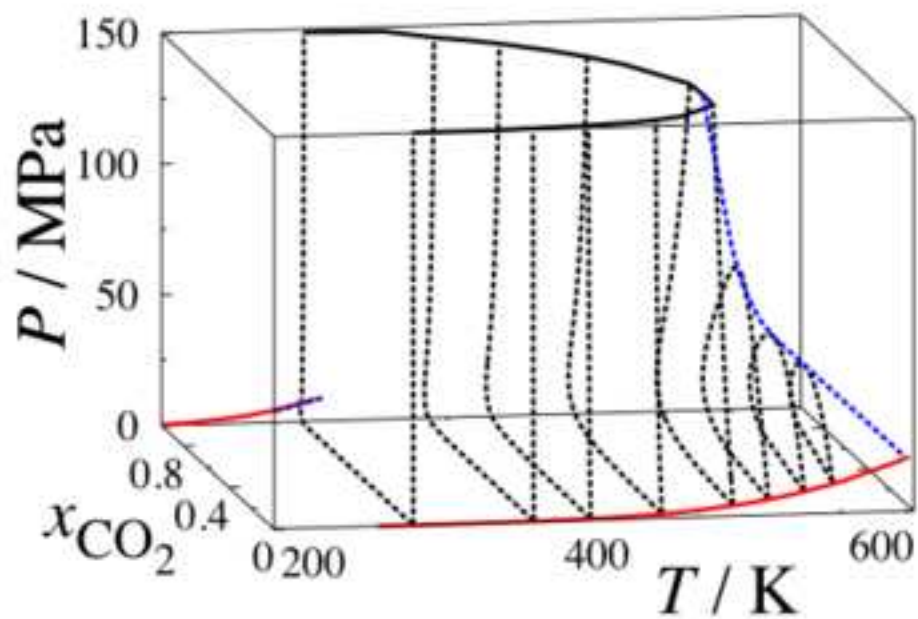
Highlights for "SAFT-γ Force Field for the Simulation of Molecular Fluids 6. Binary and ternary mixtures comprising water, *n*-alkanes, and carbon dioxide" by O. Lobanova, A. Mejia, G. Jackson and E. A. Müller

- Coarse-grained force fields for mixtures of water, carbon dioxide, and n-alkanes
- SAFT-γ parameters can be used both in EoS calculations and molecular simulations
- Single binary interaction parameter allows for description of VLE, VLLE, LLE